Geophysical Journal International

Geophys. J. Int. (2014) **198,** 637–655
Advance Access publication 2014 May 31
GJI Seismology

doi: 10.1093/gji/ggu071

Rayleigh wave tomography of the British Isles from ambient seismic noise

Heather Nicolson,[1] Andrew Curtis[1] and Brian Baptie[2]

[1]*School of Geoscience, University of Edinburgh, West Mains Road, Edinburgh EH9 3JW, UK*
[2]*British Geological Survey, Murchison House, West Mains Road, Edinburgh EH9 3LA, UK. E-mail: bbap@bgs.ac.uk*

Accepted 2014 February 21. Received 2014 February 18; in original form 2013 August 7

SUMMARY

We present the first Rayleigh wave group speed maps of the British Isles constructed from ambient seismic noise. The maps also constitute the first surface wave tomography study of the crust under the British Isles at a relatively high resolution. We computed interferometric, interstation Rayleigh waves from vertical component records of ambient seismic noise recorded on 63 broad-band and short-period stations across the UK and Ireland. Group velocity measurements were made from the resulting surface wave dispersion curves between 5 and 25 s using a multiple phase-matched filter method. Uncertainties in the group velocities were computed by calculating the standard deviation of four dispersion curves constructed by stacking a random selection of daily cross-correlations. Where an uncertainty could not be obtained for a ray path using this method, we estimated it as a function of the interreceiver distance. Group velocity maps were computed for 5–25-s period using the Fast Marching forward solution of the eikonal equation and iterative, linearized inversion. At short and intermediate periods, the maps show remarkable agreement with the major geological features of the British Isles including: terrane boundaries in Scotland; regions of late Palaeozoic basement uplift; areas of exposed late Proterozoic/early Palaeozoic rocks in southwest Scotland, northern England and northwest Wales and, sedimentary basins formed during the Mesozoic such as the Irish Sea Basin, the Chester Basin, the Worcester Graben and the Wessex Basin. The maps also show a consistent low-velocity anomaly in the region of the Midlands Platform, a Proterozoic crustal block in the English Midlands. At longer periods, which are sensitive velocities in the lower crustal/upper mantle, the maps suggest that the depth of Moho beneath the British Isles decreases towards the north and west. Areas of fast velocity in the lower crust also coincide with areas thought to be associated with underplating of the lower crust such as Northern Ireland, the eastern Irish Sea and northwest Wales.

Key words: Interferometry; Surface waves and free oscillations; Seismic tomography; Crustal structure.

1 INTRODUCTION

The development of seismic interferometry theory over the last decade allows seismologists to extract useful information from the ambient seismic noise field, which is typically otherwise removed from seismic data (Campillo & Paul 2003; Wapenaar 2003, 2004; van-Manen *et al.* 2006; Wapenaar & Fokkema 2006). So-called virtual source interferometry, which we apply here, allows us to estimate the elastic Green's function between two seismic receivers as if one had actually been a source which was recorded by the other. This is constructed from cross-correlations of long recordings of ambient seismic noise. Since the dominant sources of ambient seismic noise such as oceanic microseisms tend to be located close to the Earth's surface, interferometry typically yields the surface wave component of interreceiver Green's functions. Once obtained, these interferometric surface waves can be analysed using traditional seismological methods.

The theory of interferometry has been discussed previously from the point of view of estimating Green's functions between receivers (Campillo & Paul 2003; Wapenaar 2003, 2004; Snieder 2004, 2007; van-Manen *et al.* 2005, 2006, 2007; Wapenaar & Fokkema 2006; Slob *et al.* 2007; Wapenaar *et al.* 2011), between sources (Hong & Menke 2006; Curtis *et al.* 2009; Tonegawa & Nishida 2010; Poliannikov & Willis 2011) and between any source and receiver pair (Curtis & Halliday 2010; Halliday & Curtis 2010; Curtis *et al.* 2012). Reviews and tutorials are given in Curtis *et al.* (2006), Wapenaar *et al.* (2010a,b) and Galetti & Curtis (2012).

In recent years, seismic interferometry and ambient noise tomography have become common place as methods used to image the Earth's crust and upper mantle on regional and continental scales. To date, the areas imaged using the method include the United States (Sabra *et al.* 2005; Shapiro *et al.* 2005; Moschetti *et al.* 2007; Bensen *et al.* 2008; Liang & Langston 2008; Lin *et al.* 2008; Lawrence & Prieto 2011; Ritzwoller *et al.* 2011), Europe (Villaseñor *et al.* 2007; Yang *et al.* 2007; Nicolson *et al.* 2012), Canada (Pawlack *et al.* 2010), Australia (Rawlinson *et al.* 2008; Arroucau *et al.* 2010; Saygin & Kennett 2010), New Zealand (Lin *et al.* 2007; Behr *et al.* 2010), Antarctica (Pyle *et al.* 2010; Luzon *et al.* 2011), China (Zheng *et al.* 2008, 2010; Li *et al.* 2009), South Korea (Kang & Shin 2006; Cho *et al.* 2007), Iceland (Gudmundsson *et al.* 2007), South Africa (Yang *et al.* 2008), the East Pacific (Yao *et al.* 2011) and the Tibetan Plateau (Yao *et al.* 2006, 2008; Li *et al.* 2009; Yao & van der Hilst 2009). However, other than in our preliminary study across Scotland (Nicolson *et al.* 2012), the method has not previously been used across the British Isles, a region with a significant Atlantic noise field.

Much of our understanding of seismic velocities in the Earth's crust under the British Isles comes from active source seismic refraction and reflection experiments such as LISPB (Bamford *et al.* 1978; Barton 1992), LISPB-D (Edwards & Blundell 1984; Maguire *et al.* 2011), CSSP and ICSSP (Bott *et al.* 1985; Jacob *et al.* 1985). Kelly *et al.* (2007) combined all publicly available deep refraction wide-angle profiles from the northwest continental shelf of Europe into a 3-D velocity model constructed on a 40 × 40 km × 2 km grid. However, the uncertainties are large for all areas away from the original refraction lines included in the input data. The subsurface of the UK has also been investigated using earthquake seismology: Arrowsmith *et al.* (2005) used teleseismic body wave tomography to identify a low-velocity anomaly in the upper mantle beneath the British Isles. Hardwick (2008) constructed 3-D seismic velocity models for England and Wales using local earthquake tomography that broadly agree with observed geology. Asencio *et al.* (2003), Tomlinson *et al.* (2006), Di Leo *et al.* (2009) and Davis *et al.* (2012) all use teleseismic receiver functions to identify features of the crust and upper mantle under the UK. By contrast, only a few limited studies have explored the use of surface waves to extract information about the structure of the crust under mainland UK.

Continental Europe experiences a relatively high rate of seismicity and has a dense coverage of seismometers, therefore it has been the subject of many surface wave tomographic studies on regional and local scales (Marquering & Snieder 1996; Curtis *et al.* 1998; Ritzwoller & Levshin 1998; Villaseñor *et al.* 2001; Pilidou *et al.* 2004; Fry *et al.* 2008; Peter *et al.* 2008; Weidle & Maupin 2008; Schivardi & Morelli 2009). While these studies have provided higher resolution images of the lithospheric velocity structure of Europe, the British Isles are usually located towards the edge of these models, and are spanned by only a small number of the seismic stations used. Hence, they are subject to data coverage and edge effects in the resulting tomographic models. Nicolson *et al.* (2012) presented Rayleigh wave maps of the Scottish Highlands derived from ambient seismic noise recorded on the Reflections Under the Scottish Highlands (RUSH-II) temporary seismometer network deployment (Asencio *et al.* 2003; Bastow *et al.* 2007). The results were consistent with other surface geological, gravitational and magnetic observations, but the lateral extent of well-resolved structure was limited to about a quarter of the Scottish mainland. In this paper, we present the first Rayleigh wave group velocity maps across most of the British Isles from ambient noise tomography. We include most available stations including a subsample of the RUSH-II stations, selected so that the station distribution across the entire spanned region has approximately homogeneous station density. This allows us to compute Rayleigh wave group velocity maps for almost the entire British Isles from ambient seismic noise.

We begin by providing a brief overview of the ambient noise tomography method and describing the station distribution used to construct the maps. We then examine the resolution of the data set using chequerboard tests and present Rayleigh wave velocity maps for a number of periods across the British Isles. Finally, we consider possible geological interpretations of the main features of the tomographic maps and make comparisons with previous studies of the region.

2 GEOLOGICAL SETTING OF THE BRITISH ISLES

The British Isles are an archipelago located adjacent to the Eurasian continental shelf in an intraplate setting. The islands were formed by the amalgamation of several fault bounded basement blocks or terranes (Bluck *et al.* 1992), during a complex geological history consisting of multiple episodes of deformation (Woodcock & Strachan 2000). Fig. 1 shows a schematic summary of the main terranes of the British Isles separated by the major regional fault structures related to orogenic events.

Plate reconstructions suggest that during the Phanerozoic the northern part of the British Isles was located at the passive margin of Laurentia, while the southern part was located at the subducting margin of Avalonia. Between 470 and 380 Ma, the Grampian, Caledonian and Acadian orogenies (Woodcock & Strachan 2000) resulted in the closure of the Iapetus Ocean and the amalgamation of the Avalonian microcontinent (which included England, Wales and South East Ireland) with the edge of the continent of Laurentia (which included Scotland and North West Ireland).

The far northwest of the British Isles are dominated by high-grade metamorphic complexes such as the Archaean Lewisian gneisses, overlain by thick Torridonian sandstones. Thick metasedimentary sequences of the Moine Supergroup overlying high-grade gneissic basement occur between the Moine thrust and the Great Glen Fault (GGF). More varied metasediments of the Dalradian Supergroup, together with abundant granite plutons form the Grampian Highlands. Palaeozoic sediments such as Old Red Sandstones and volcanics of Devonian and Carboniferous age occur in the Midland Valley, south of the Highland Boundary Fault. Material from an accretionary prism on the southern boundary of Laurentia formed the Southern Uplands terrane, a thick sequence of Ordovician and Silurian sandstones and mudstones.

Southern Britain formed part of eastern Avalonia, a small crustal block formed during the Neoproterozoic at the eastern, active margin Gondwana. Island arc volcanoes and marginal basins led to the formation of sequences of volcanosedimentary rocks; Avalonia and Armorica rifted of East Gondwana. However, much of the evidence of the Avalonian terrane is covered by younger rocks across England and Wales.

A series of orogenic events during the Palaeozoic amalgamated these different terranes. The Caledonian Orogeny led to intense deformation and significant magmatism in Scotland. Collision of the Armorican microcontinent with Avalonia occurred during the Acadian event (400 Ma), with the (now largely concealed) Midland Platform possibly forming a rigid indentor.

The main collision of Gondwana with Laurentia led to the Variscan orogeny in northwest Europe, forming a mountain belt

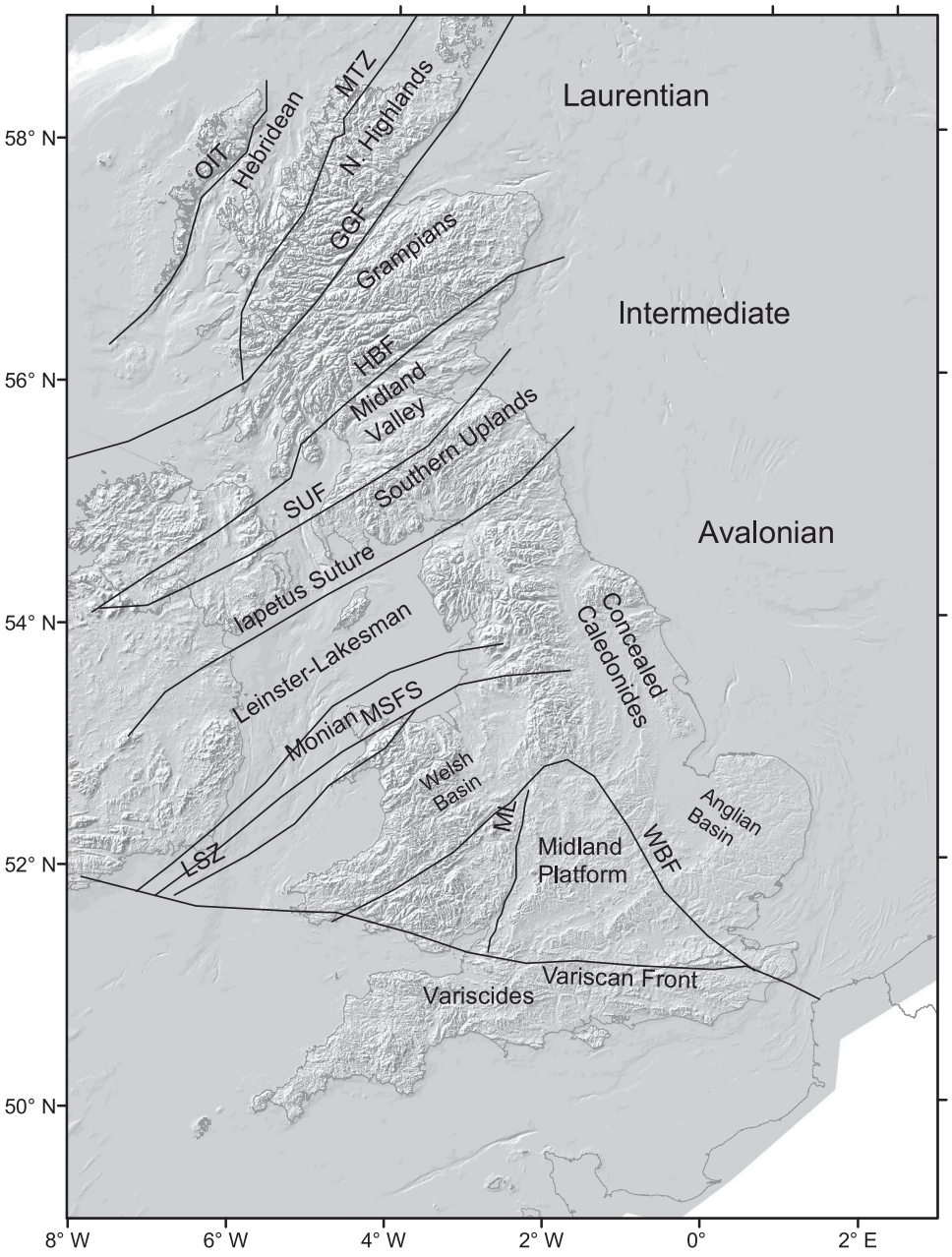

Figure 1. Schematic map of the main geological terranes of the British Isles. Solid black lines represent the major tectonic boundaries and unconformities. WBF, Welsh Borderland Fault zone; LSZ, Lleyn Shear Zone; MSFS, Menai Straits Fault System; ML, Malvern Lineament; PL, Pennine Line; SUF, Southern Uplands Fault; HBF, Highland Boundary Fault; GGF, Great Glen Fault; MTZ, Moine Thrust Zone; OIF, Outer Islands Fault. After Woodcock & Strachan (2000).

in North America and Europe. Evidence of this mountain belt in the British Isles can be found in the Variscides of southwest England, which are separated from the more weakly deformed rocks to the north by the Variscan Front. Towards the end of the Variscan orogeny, a large granite batholith was emplaced in Devon and Cornwall. By the early Permian, the components of the British Isles crust had amassed approximately into their present day relative positions as part of the Pangea supercontinent.

During the Jurassic and Cretaceous, Pangea began to split apart. The associated opening of the Atlantic caused crustal extension in the British Isles, forming large rift basins throughout the mainland and North Sea. Although these rift basins were formed by subsidence, the British Isles have experienced up to 3 km (locally) of uplift and exhumation. A possible cause of this is thought to be underplating of buoyant igneous material due to the North Atlantic opening over the Icelandic plume (Brodie & White 1994; Nadin *et al.* 1995, 1997; Bijwaard & Spakman 1999; Kirstein & Timmerman 2000; Foulger 2002; Bott & Bott 2004; Anell *et al.* 2009). However, Hillis *et al.* (2008) argue that the crust has been modified by contractional deformation which has caused some of the observed Cenozoic uplift. The western parts of the British Isles form part of the North Atlantic Tertiary Igneous Province (NATIP), a large igneous province composed of flood basalts, sill and dyke intrusions stretching from West Greenland to Denmark. In the British Isles, features of the NATIP are particularly evident in the west of Scotland and Northern Ireland.

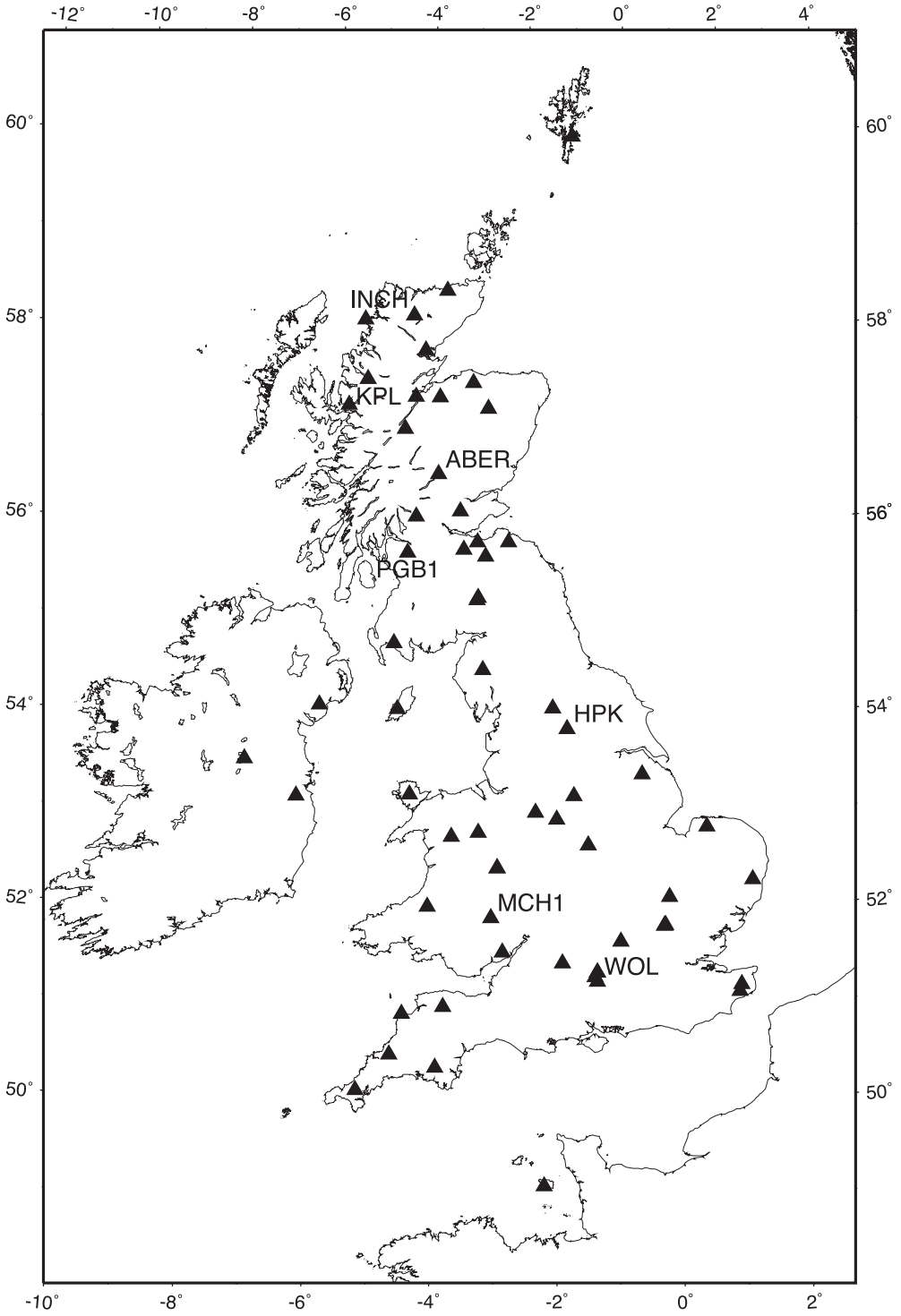

Figure 2. Location map of stations (black triangles) used to construct Rayleigh wave velocity maps for the British Isles.

The geology of the British Isles is therefore highly heterogeneous with multiple episodes of deformation. Although a number of previous studies suggest that lateral changes in seismic velocity are small, herein we show that this is not the case, and that some of the key geological features such as terrane boundaries, igneous and metamorphic complexes and sedimentary basin are well resolved by Rayleigh wave speed maps across the region.

3 DATA AND METHOD

The network of seismic stations used in this study is shown in Fig. 2. We have combined data from broad-band and short-period instruments from the British Geological Survey network with broad-band instruments from the RUSH-II experiment (Asencio *et al.* 2003; Bastow *et al.* 2007), British Isles Seismic Experiment (Davis 2010), Atomic Weapons Establishment UKArray (Douglas 2001)

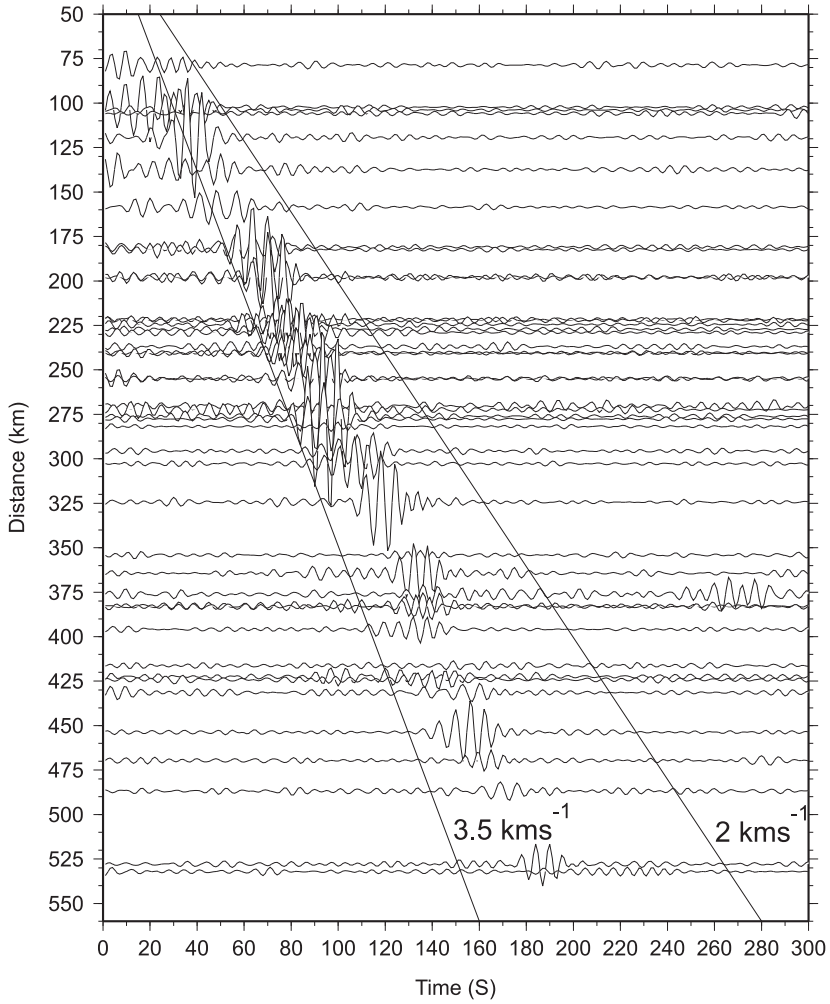

Figure 3. Cross-correlation gather for station HPK (Fig. 2). Solid lines represent propagation velocities of 2 km s^{-1} (right) and 3.5 km s^{-1} (left). All waveforms are bandpassed between 5 and 10-s periods.

and Observatories and Research Facilities for European Seismology (ORFEUS) network.

In this study, we follow the same data processing procedure as Nicolson *et al.* (2012), which we summarize here. Continuous, vertical component noise data for each station were cut into segments of 24 hr length. The mean, linear trend and instrumental response were removed from each segment then the data were decimated to a sampling rate of one sample per second. Next, the day segments were temporally normalized to reduce the impact of large amplitude and non-stationary events such as earthquakes on the cross-correlation process. Bensen *et al.* (2007) describe various methods of temporal normalization and favour using a running absolute mean since it offers greater adaptability to individual data sets, for example noise data recorded within an area of high seismicity. However, this method is computationally expensive and on testing we found no significant difference in results between this and the 1-bit normalization method where only the sign of the noise data is retained (Bensen *et al.* 2007). We therefore adopted the latter method. The 1-bit day segments were then spectrally whitened in order to broaden the spectrum of the ambient noise data, and thus broaden the frequency content of the resulting cross-correlations. The daily time-series were inspected visually and days with a significant amount of off-time (approximately greater than 20 per cent) or containing obvious glitches such as spikes were discarded.

After all of these pre-processing steps were applied, cross-correlations between each of the resulting day segments were computed for every possible station pair. The resulting cross-correlations are two-sided functions, where the signal at positive and negative lag times (i.e. causal and acausal components) represents energy travelling in opposite directions between a pair of stations. Where the cross-correlation function is asymmetric around zero delay time, the ambient noise can be inferred to have travelled predominantly in one direction between the stations. This is a common phenomenon of cross-correlations across the British Isles since seismic noise derived from Atlantic Ocean microseisms is the dominant ambient energy source (Nicolson *et al.* 2012).

Fig. 3 shows a cross-correlation gather (only one side of the cross-correlations are shown here) for station HPK (Fig. 2). In this case, station HPK is used as the virtual source and time-series are plotted as a function of virtual source–receiver separation. Increasing offset between the virtual source and receivers causes an increasing delay in the arrival time of the propagating seismic energy. This is clearly observable in Fig. 2. The two solid lines in Fig. 2 represent propagation velocities of 2 and 3.5 km s^{-1} which bracket typical surface wave velocities in continental crust. The interferometrically constructed surface wave estimates shown in Fig. 3 therefore moveout with realistic surface wave velocities.

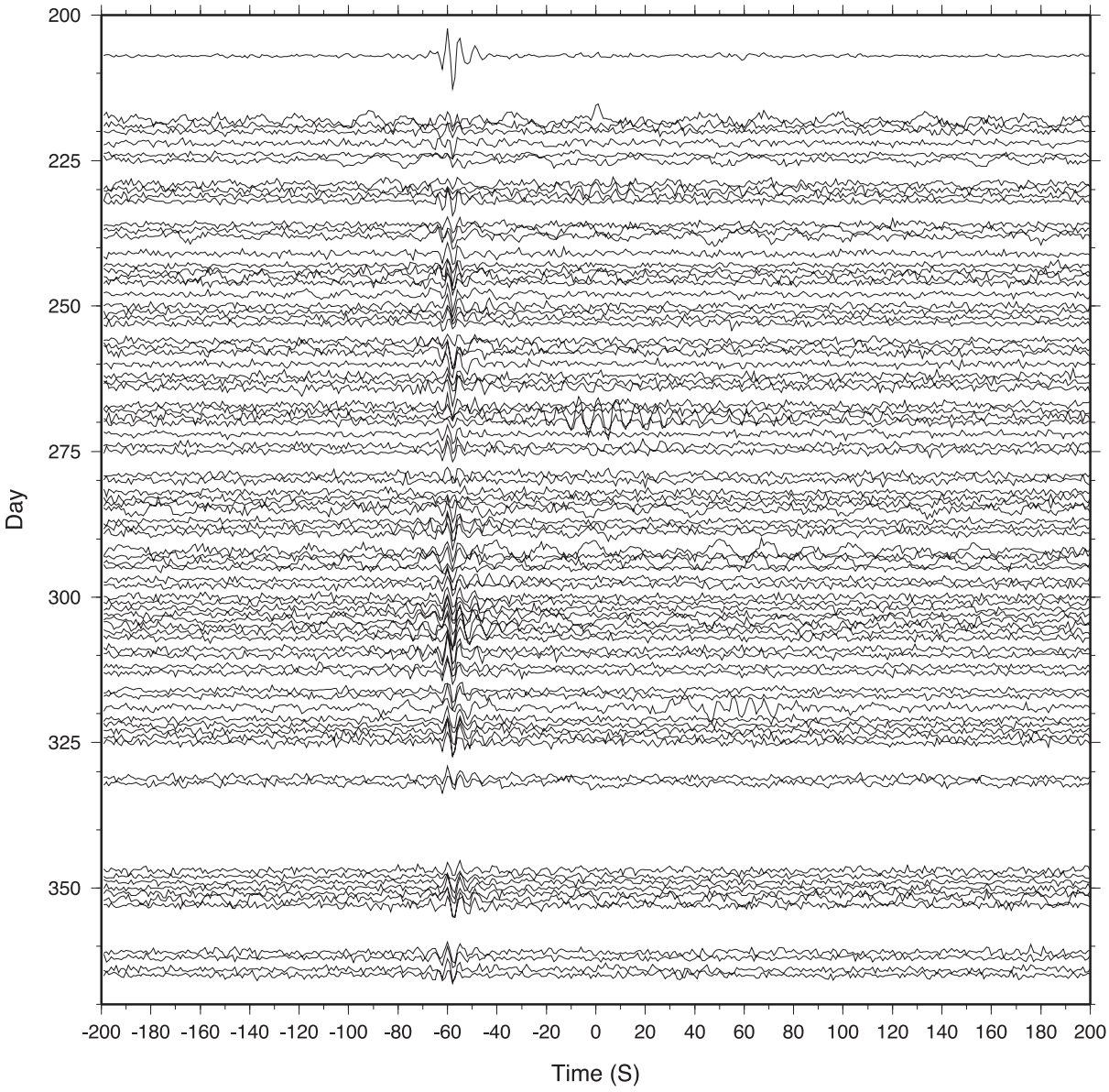

Figure 4. Daily cross-correlations for 2001 between ABER and INCH. The *y*-axis denotes the day of year of the corresponding time-series. Top: result of stacking all daily cross-correlations.

To obtain the best results from seismic interferometry, a long time-series should be used (van-Manen *et al.* 2006; Bensen *et al.* 2007). However, processing, storing and cross-correlating time-series of several years in length would be extremely inefficient. Therefore, previous studies have used time-series of shorter length, typically 12 or 24 hr, as we have in this study. Stacking the resulting daily cross-correlations gives a result equivalent to cross-correlating over the entire time period and involves adding the unweighted, daily cross-correlations for a station pair together. Fig. 4 shows a number of daily cross-correlations between stations ABER and INCH on the RUSH-II seismometer network (see Fig. 2). The result of stacking (summing) all of these cross-correlations is shown at the top of the figure. Surface waves can be observed to arrive consistently at around −60 s on the daily cross-correlations and emerge clearly on the stacked result.

On average, stacking over an increasing number of days improves the signal-to-noise ratio of the stacked cross-correlations. Fig. 5 shows an example of the emergence of the Rayleigh wave signal, and improvement of the signal-to-noise ratio, as the number of daily cross-correlations included in a stack increases from 1 day to 1 week, 1 month and 229 days. As the stacking time increases, the coherent arrivals are enhanced whereas incoherent noise becomes progressively suppressed.

The waveforms in Fig. 5 also clearly demonstrate the asymmetry that is typical of ambient noise cross-correlations in the British Isles (note that time 0 s is in the centre of the time-series). Since we generally do not know whether the causal or acausal part contains more useful information, we combine both parts by summing the causal part with the time reverse of the acausal part. This summed component is then considered to be our estimate of the virtual, interreceiver, surface wave seismogram. It is worth noting, however, that by using the summed component in this way there is potential for some information to be lost on some paths. Only 1500 s of the symmetric component was retained since this provides a time window more than long enough for energy propagating along the longest UK interreceiver path to arrive.

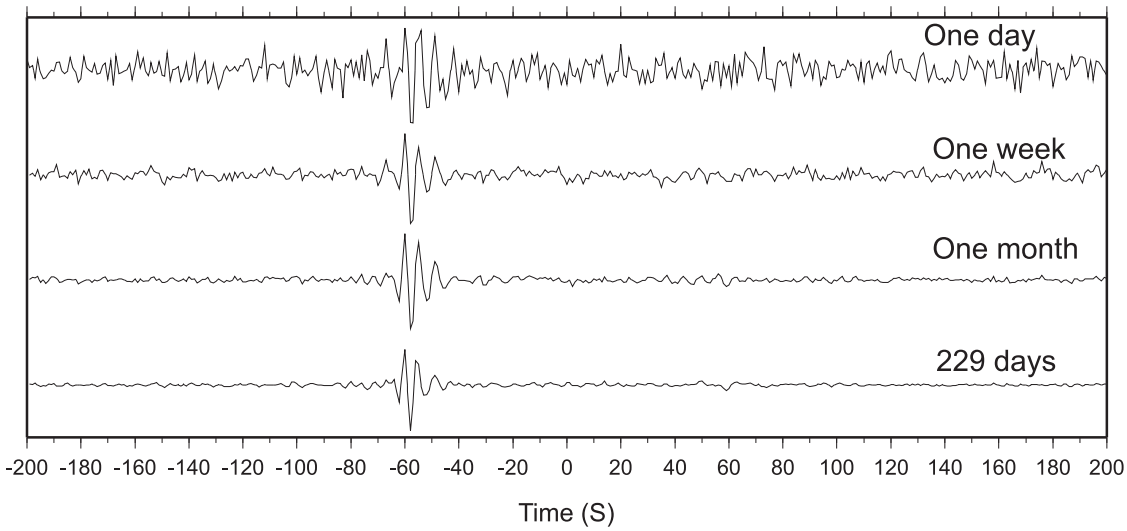

Figure 5. Emergence of Rayleigh waves for stacks over increasingly longer time periods between ABER and INCH.

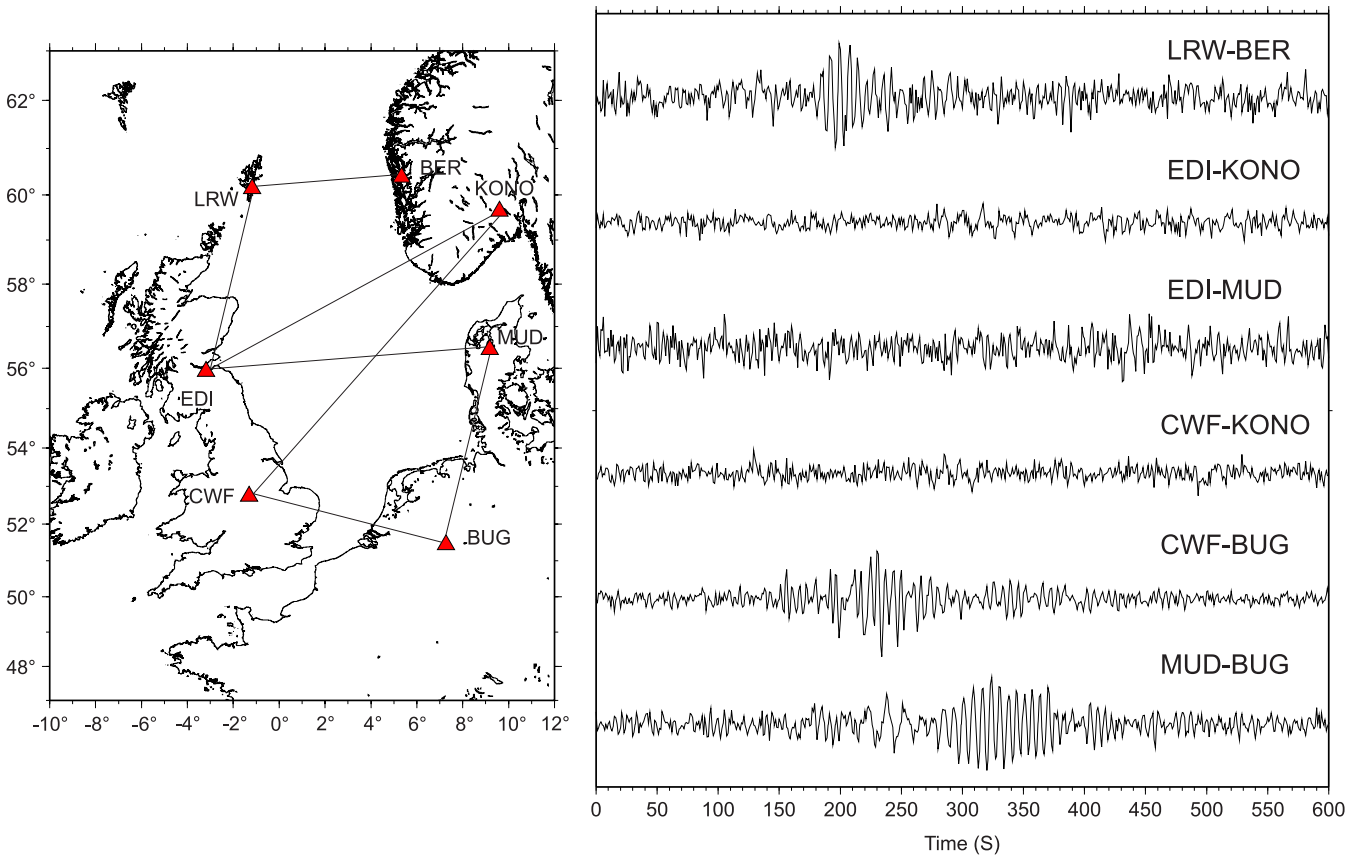

Figure 6. Comparison of paths crossing different parts of the North Sea. (a) Station location map, ray paths between stations represented by solid black lines. (b) Total cross-correlation stacks for the ray paths shown in (a).

In this study, we originally included stations located near to the coast of continental Europe with the aim of also covering the North Sea region in our tomographic maps. However, we found that our surface wave Green's functions across the North Sea have very low signal-to-noise ratios. This is illustrated in Fig. 6. For some paths crossing the central and northern North Sea, no coherent surface waves were obtained even when (as here) multiple years of data were stacked. For example, no surface waves were observed for paths crossing the central North Sea EDI-KONO, EDI MUD and CWF KONO. The results are slightly improved for paths crossing the southern North Sea, for example, CWF BUG and BUG MUD, although these paths are still poor compared with overland paths. A reasonable result was also obtained for path LRW BER which crosses the Viking Graben in the northern North Sea. We therefore chose to exclude North Sea paths from subsequent inversions in this study, but return to this issue in Section 6.

Interferometric surface waves are dispersive, that is, different frequencies within the surface wave packet travel at different speeds

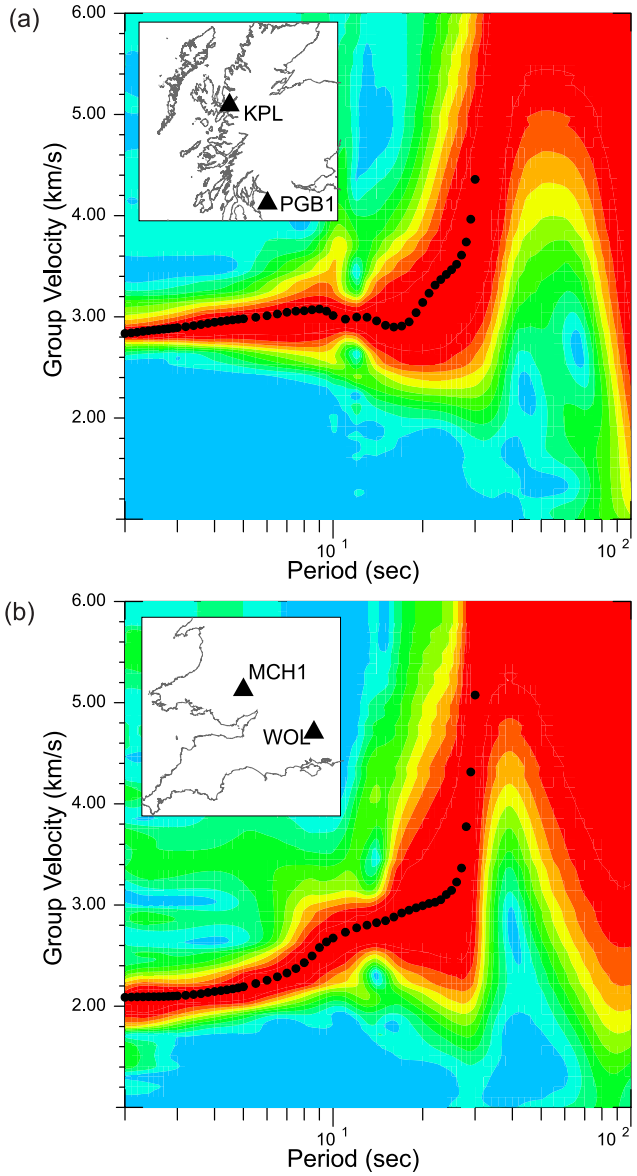

Figure 7. Multiple phase-matched filter results along with the picked Rayleigh wave group velocities (black circles) from Green's functions calculated for station pairs (a) KPL–PGB1 in northwest Scotland and (b) MCH1–WOL in the south of England.

since they are sensitive to structure at different depths. Longer period surface waves are sensitive to deeper parts of the lithosphere, and since seismic velocity generally increases with depth these waves are typically observed to arrive first on a seismogram. Surface wave dispersion is usually described by a dispersion curve which is a plot of frequency or period against velocity. By splitting a surface wave into its constituent frequencies and measuring their speeds, we can infer information about the Earth's subsurface velocity structure. Rayleigh waves can be described by a discrete series of modes (Aki & Richards 2002). We focused on the fundamental Rayleigh wave mode since this is normally the most clearly identified on interferometric seismograms. We applied the multiple phase-matched filter method of Herrmann (2005) to measure dispersion of the interferometric surface waves (Fig. 7).

At this stage, stacked cross-correlations between stations with a separation of less than 50 km were rejected since in the period range considered, useful results were not produced by station pairs that are separated by smaller distances. Furthermore, paths where the signal-to-noise ratio was poor and a corresponding dispersion curve could not be picked were also rejected. Dispersion curves were picked manually for the remaining paths over as wide a period range as possible.

Although the dispersion curves are plotted as frequency versus velocity, the quantity actually measured using the multiple phase-matched filter method is the traveltime of the peak of the Rayleigh wave envelope for narrow-band wave groups around each frequency. Such traveltimes measured from stacks over the total time period for which noise data were available were used as the input traveltimes for tomographic inversion. A significant advantage of seismograms from seismic interferometry over earthquake derived seismograms is that measurements should be repeatable in time. This allowed us to estimate traveltime uncertainties from the standard deviation of traveltimes picked from dispersion curves calculated for four, independent stacks of randomly chosen daily cross-correlations.

However, for a number of the paths used in this study, there was sometimes not a sufficient number of daily cross-correlations to estimate traveltime uncertainties using the method described above, although these appeared to provide good quality dispersion curves. At some periods, removing these paths completely from the data set significantly reduced the path coverage over the study area. One control on uncertainty is the interstation distance. This can be observed, for example, in Fig. 3 where for short interreceiver paths the surface wave group energy is not always readily identifiable as being away from zero time, and for long paths the amplitude may be reduced. Therefore, we aimed to determine the relationships between interstation distance and traveltime uncertainty, and use this to estimate the traveltime uncertainty for paths without direct uncertainty estimates.

Since the relationship between interstation distance and traveltime uncertainty was observed to be only weakly correlated in the UK overall, we doubled the uncertainty estimates calculated using this method to make them more conservative. To check that these paths do not create undue structural changes to the Rayleigh wave maps, we performed all subsequent inversions twice: first for paths with a direct associated uncertainty measurement only, and secondly also including paths with uncertainties estimated from their interstation distance. The maps using all paths (i.e. those with both direct uncertainty measurements and indirect uncertainty estimates from distance) generally agree extremely well with the features of the maps using well-constrained paths only, hence, we are reasonably confident that structure shown by these maps is realistic.

Finally, to show that the group velocity dispersion curves are reasonable and show agreement with the subsequent tomography results, we carry out inversions using surface wave Green's functions from two station pairs to determine simple 1-D velocity models for each path. Fig. 7 shows the multiple phase-matched filter results along with the picked Rayleigh wave group velocities (black circles) for Green's functions calculated for station pairs KPL–PGB1 (Fig. 7a) in northwest Scotland and MCH1–WOL (Fig. 7b) in the south of England. Each dispersion curve is well constrained and shows quite different characteristics, suggesting that the average seismic velocity structure along beneath each path is quite different.

We use a linearized least-square inversion algorithm (Russell 1987) to determine shear velocity, V_s, as a function of depth from the group velocity dispersion curve. The algorithm iteratively varies the layered seismic velocity model until it best fits the observed data. We use a simple starting model in which both the Crust

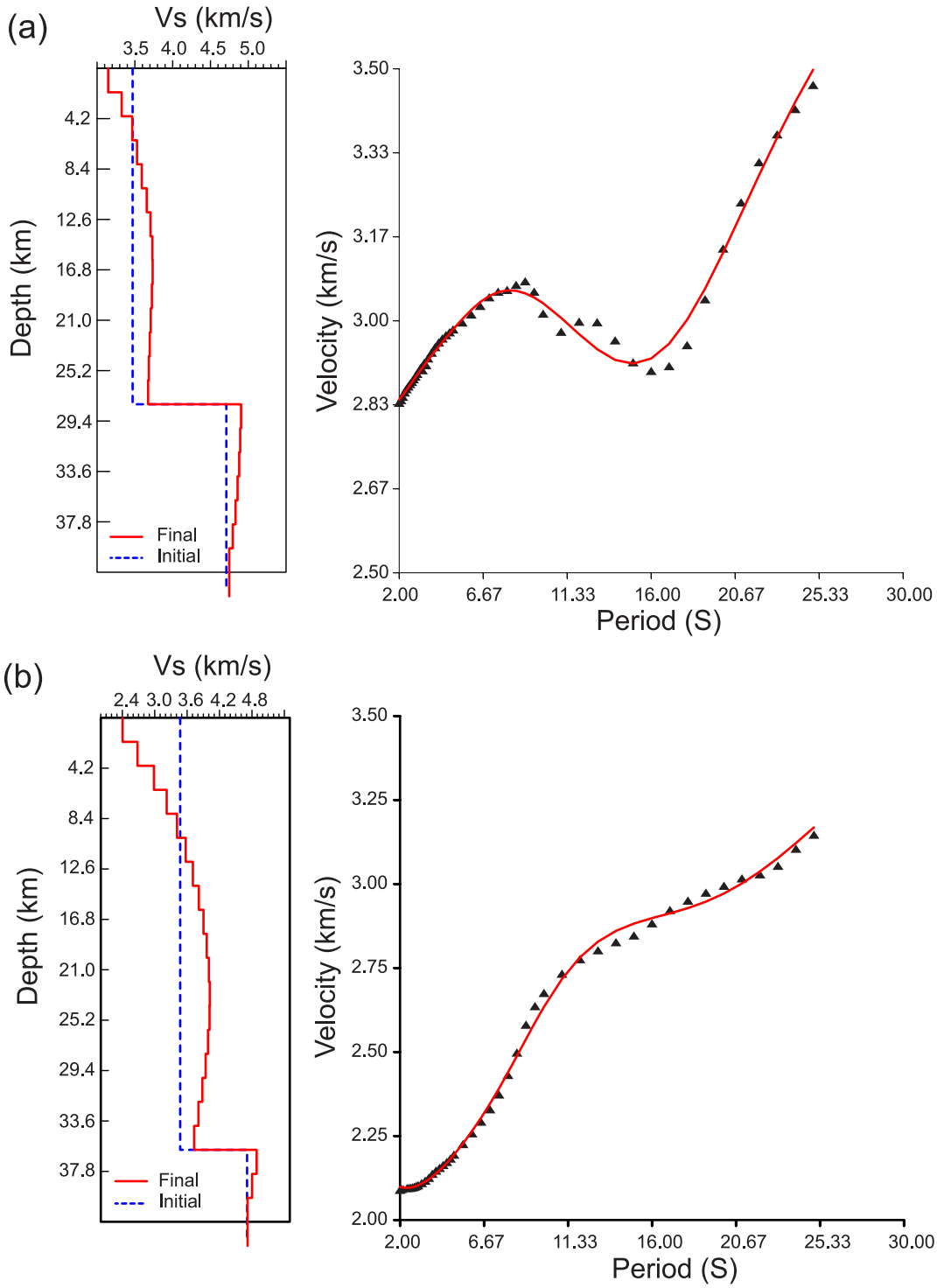

Figure 8. Results of the 1-D inversion of the Rayleigh wave group velocity dispersion curves for station pairs (a) KPL–PGB1, and (b) MCH1–WOL. The black triangles show the observed values of velocity at each period while the red lines show the dispersion curve for the best-fitting velocity model. The velocities models are shown on the left-hand side for both the final (red) and initial (blue) models.

and Mantle have uniform velocities, parametrized by a number of layers each with a thickness of 2 km. In addition, we tried a number of different starting models in which the overall thickness of the crust varied between 26 and 36 km, which are though to span a typical range of values for the UK crust. The results did not vary greatly between inversions from different starting models, and the best-fitting results are shown in Fig. 8. The black triangles show the observed values of velocity at each period while the red lines show the dispersion curve for the best-fitting velocity model. The velocities models are shown on the left-hand side for both the final and initial models. Even though some small group velocity variations are not fit exactly, both models provide a reasonable fit to the observations. The results show that velocities in the top 10 km are significantly lower between MCH1 and WOL than between

KPL and PGB1. This is consistent with the geological setting, with Proterozoic metamorphic basement between KPL and PGB1, whereas the path between MCH1 and WOL1 traverses the Worcester Graben, a Mesozoic basin. At depths greater than 10 km, the models are similar, both showing slight increases in velocity. However, the thickness of the Crust between MCH1 and WOL appears to be significantly greater (36 km) than between KPL and PGB1 (26 km). This is consistent with previous studies which suggest that the crust is significantly thicker in the south than in the north of the UK due to the general southeastward dip of the UK lithosphere. Of course, these two velocity structures are uncertain due to the data measurement uncertainties, and are likely to be biased to some extent by our choice of how to fix the *P* velocity and density. Nevertheless, our purpose here was to demonstrate that the group velocities that we measure across different periods are physically consistent with our expectations of the subsurface geology, and that has been achieved by the quality of the match to the measured data in each case.

4 RAYLEIGH WAVE TOMOGRAPHY

We applied the iterative, non-linear surface wave tomography scheme of Rawlinson *et al.* (2006) to produce maps of Rayleigh wave velocity for the British Isles. First, the Fast Marching method of Sethian & Popovici (1999), a grid-based eikonal equation solver, is used to calculate traveltimes through the model space. Next, Rawlinson *et al.* (2006) solve the inversion step using the linearized subspace inversion scheme of Kennett *et al.* (1988). The Fast Marching method and subspace inversion method are then applied iteratively to account for the non-linearity of the tomography problem. In ambient noise tomography problems, a travel path potentially exists between every pair of seismic receivers although not every pair will have a measured traveltime value associated with it. This situation leads to a large, underdetermined inverse problem. However, the tomographic method of Rawlinson *et al.* (2006) that we use is regularized (as explained below) such that it remains stable and efficient under these conditions.

Before performing a tomographic inversion with real surface wave traveltime data it is important to understand how well the subsurface structure might be resolved by the geometry of stations and virtual sources shown in Fig. 2. Similarly to Nicolson *et al.* (2012), we did this by generating synthetic data for each of a series of chequerboard models which represent an imaginary Earth's group velocity structures, calculating a solution model using the synthetic data and our chosen tomography scheme, then comparing the solution velocity models with the synthetic earth models. Although these tests formally only check the extent to which a chequerboard model can be resolved, we expect them to give at least a basic impression of the variation in resolving power of the data at each period and across different geographic areas.

Synthetic interstation traveltimes were calculated through a velocity model of alternating faster and slower velocity cells for the same station pairs as are available for each period in the real data set. These synthetic traveltimes were then treated as the observed traveltimes to determine the resolving power of the given geometry for many combinations of damping and smoothing parameters. Only ray paths for which a real traveltime measurement at the specified period exists have their equivalent synthetic traveltime included in the corresponding chequerboard test. In addition, we associated these synthetic traveltimes with the corresponding uncertainties estimated from the real data for each path; this ensures that paths that will be downweighted (due to higher uncertainty) in the real-data inversions are also downweighted in the synthetic chequerboard tests.

In this paper, we present Rayleigh wave speed maps for 5, 6, 8, 10, 12, 15, 18, 20 and 25-s periods. Fig. 9 shows the results of synthetic chequerboard resolution tests for 5-s period and a variety of chequerboard grid sizes from 2° to 0.25° cell side lengths, using all paths (i.e. combining those with uncertainty measurements and those with uncertainty estimates from interstation distance). We use a geographic (latitude–longitude) grid, in keeping with other surface wave studies (e.g. Yang *et al.* 2007). Since, the geographical area in this study is small, we do not expect this to affect the results.

For all chequerboard tests, there is no resolution across western Ireland, the North Sea and mainland Europe as expected, since these areas are outside of the data coverage in all cases. At 5-s period, the $2^\circ \times 2^\circ$ and $1^\circ \times 1^\circ$ cell chequerboards (Figs 9b and d) are relatively well resolved. For the $1^\circ \times 1^\circ$ cell chequerboard, some smearing occurs towards the edges of the resolvable area, particularly in the Irish Sea, English Channel, along the east coast mainland and across the Northern Isles. At a cell size of $0.5^\circ \times 0.5^\circ$ (Fig. 9f), the resolution has degraded across most of the British Isles and smearing at the edges is more pronounced. This smearing is a result of both the limited station density and the particular station geometry. Some structure is still resolved however in southern Scotland and the English Midlands. For a $0.25^\circ \times 0.25^\circ$ cell size (Fig. 9h), the resolution across the whole of the British Isles has been almost completely lost and we conclude that this is the lower limit of resolution.

We choose the node spacing of our inversion grid to be much smaller than the minimum length-scale that is well resolved by the data. This ensures that we minimize any spectral leakage of true Earth structures at length-scales smaller than the resolvable feature size into our maps (Trampert & Snieder 1996). By analysing chequerboard test results for all periods, the inversion grids chosen for our periods of interest are shown in Table 1.

Note that there are also potential limitations in the results presented in this paper due to the use of ray theory. In general, the validity of ray theory is breached in this study as the wavelength of the signal tends to the length-scale of the structural heterogeneity. Some of the chequerboard tests that we performed involved cells with length-scales smaller than the approximate wavelength of the corresponding period. It is important to keep this limitation in mind when interpreting structures in the final tomography maps, since ray theory imposes a lower bound on the length-scale of structure that can be resolved at each period. In future studies, it would be advantageous to account for these so-called finite-frequency effects in the inversions (Ritzwoller *et al.* 2002).

5 RAYLEIGH WAVE GROUP VELOCITY MAPS

Using the 2-D iterative, non-linear tomography scheme described above, we inverted Rayleigh wave group velocity traveltime data sets for 5, 6, 8, 10, 12, 15, 18, 20 and 25-s periods. The inversion grid spacing in each case was chosen according to Table 1, and an appropriate (finer) propagation grid was chosen by trial and error which minimized the computation time of the forward part of the problem using the Fast Marching method without significantly altering the features of the tomographic maps. The starting model at

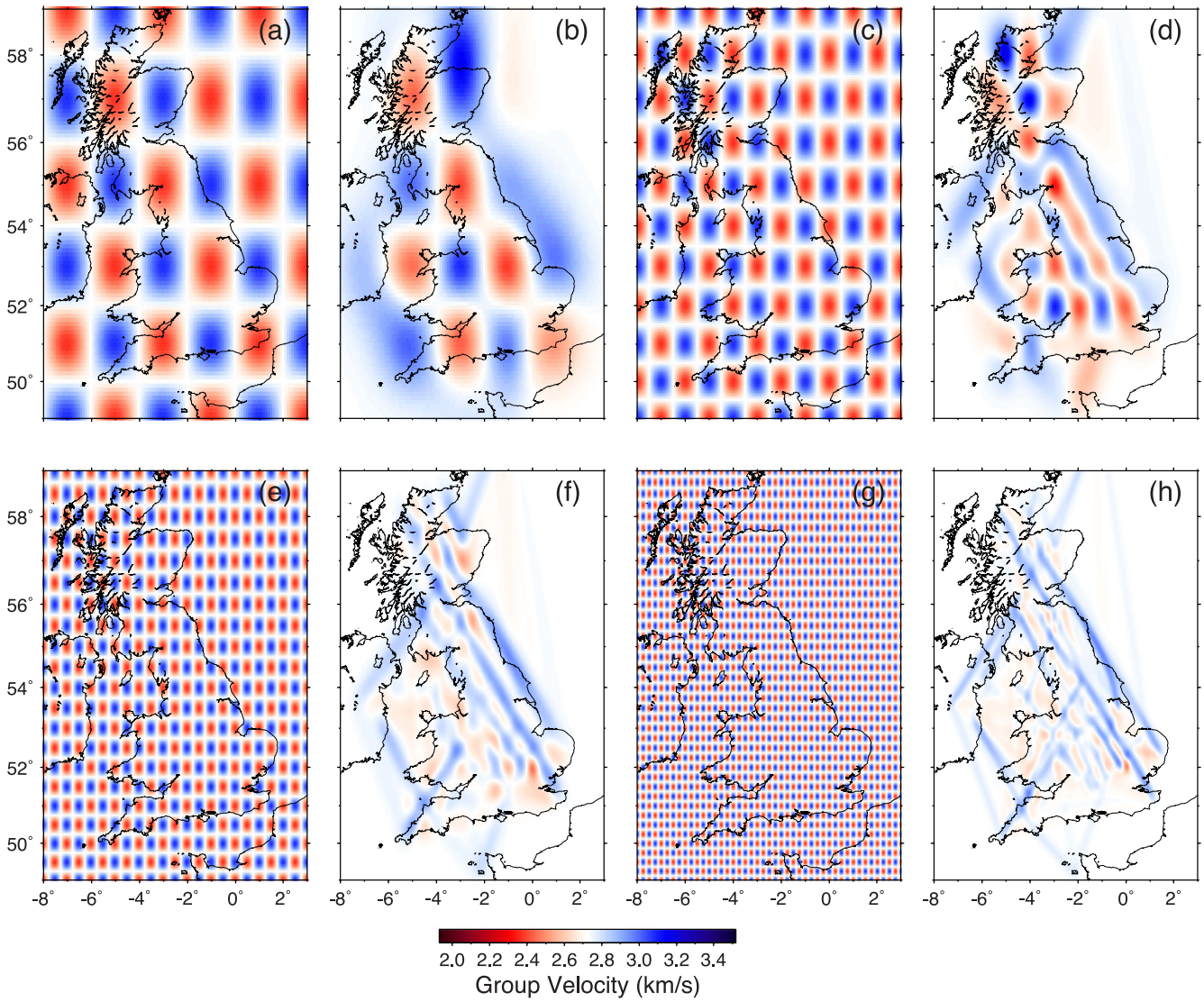

Figure 9. Chequerboard resolution test results at 5-s period, (a) synthetic model with 2° × 2° chequerboard cells; (b) inversion results for 2° × 2° chequerboard model; (c) synthetic model with 1° × 1° chequerboard cells; (d) inversion results for 1° × 1° chequerboard model; (e) synthetic model with 0.5° × 0.5° chequerboard cells; (f) inversion results for 0.5° × 0.5° chequerboard model; (g) synthetic model with 0.25° × 0.25° chequerboard cells; (h) inversion results for 0.25° × 0.25° chequerboard model.

Table 1. Inversion grid node spacings for each period considered.

Period (s)	Inversion grid
5	0.125° × 0.125°
6	0.125° × 0.125°
8	0.125° × 0.125°
10	0.25° × 0.25°
12	0.25° × 0.25°
15	0.25° × 0.25°
18	0.25° × 0.25°
20	0.5° × 0.5°
25	0.5° × 0.5°
30	0.5° × 0.5°

Table 2. Average Rayleigh wave group velocity for each period considered.

Period (s)	Average velocity (km s^{-1})
5	2.727
6	2.763
8	2.831
10	2.875
12	2.893
15	2.972
18	2.968
20	2.996
25	3.076
30	3.169

each period was homogeneous where the velocities were chosen to be the average measured across the UK for that period. The average velocities for each period are given in Table 2. Note that the average velocity generally increases with increasing period.

Tomographic maps were computed for many different combinations of damping and smoothing parameters and the weighted root mean square (rms_W) of the data residuals was calculated for each map. The rms_W is a dimensionless measure of the post-inversion,

normalized misfit of the synthetic traveltime data corresponding to the solution model that takes account of the *a priori* data uncertainties:

$$rms_{\mathrm{W}} = \sqrt{\frac{1}{N}\sum_{i=1}^{N}\frac{x_i^2}{\sigma_i^2}}, \quad (1)$$

where N is the number of ray paths, and x_i and σ_i are the traveltime residual and uncertainty associated with each ray path i. We can assume that if the value of rms_{W} is significantly greater than 1 then the data fit is potentially biased by the choice of regularization parameters rather than real Earth structure. However, if the value of rms_{W} is around 1 then we can say that, to within data uncertainties, the earth model solution fits the observed data.

Initial inversions tend to yield high rms_{W} values. The highest residual paths are then removed from the data set and the inversions are repeated. This process of path removal and inversion is iterated until the corresponding rms_{W} value at that period drops below an acceptable threshold. The justification of this strategy is that due to any of a variety of reasons (station timing errors, statistics of small numbers since only four independent picks of velocities were used to estimate uncertainties, consistent bias in the ambient noise field, small-scale heterogeneity around the seismometer stations that cannot be modelled by our gridded parametrization, etc.) the data uncertainties as estimated herein may not truly represent the uncertainty on some data values. When estimated uncertainties are significantly lower than either the true uncertainties or the bias, such data dominate the rms_{W} values and also potentially the inversion results. The main features of the computed maps are generally unaffected by the removal step, other than to remove a few obviously anomalous streaks of high or low velocity that were produced along single rays corresponding to the anomalous data that were removed. Thus, we are confident that anomalous data are unlikely to contaminate the final maps, and that this step did not unduly bias our results.

Fig. 10 shows a grid of resulting Rayleigh wave group speed maps for different combinations of damping and smoothing values at 5-s period. Maps located within the blue contour on the grid are not considered since they have had zero damping and smoothing applied and give results that are geologically unrealistic. Maps located within the red contour have corresponding rms_{W} values that are roughly acceptable and provide geologically sensible results. Note also that the main features of these maps are robust to different choices of regularization parameters. We can therefore be fairly confident that they are likely to be due to real Earth structure as resolved by the data.

For a number of inversions, it was difficult to get the rms_{W} values for the maps to reduce to close to 1. This was a particular problem at lower periods. In some cases, it was impossible to reduce the rms_{W} value to approximately 1 without removing over 80 per cent of the paths from the traveltime data set and at this stage all interesting features are lost from the maps. Therefore, we decided to slightly relax our requirement to have rms_{W} values close to 1 for these problematic maps in order to retain more paths, hence the more liberal choice of red contour in Fig. 10.

This problem is itself an interesting conclusion since it most likely means that the method we have used to measure uncertainty is not always giving reliable results. This method appeared to work for the study across the Scottish Highlands (Nicolson *et al.* 2012), but seems to have flaws when applied to the more extensive area considered here. What data error actually means for inversions is the difference between the predicted (modelled) and measured data, in our case traveltimes. This error therefore includes: (i) the measurement error (i.e. the error involved in measuring the observed traveltimes), and (ii) the modelling error, which is due to the inability of the inversion scheme to model the observed data. The modelling error will be affected by factors such as the parametrization of the problem and the physics involved with modelling the predicted data not being exactly appropriate for the specific problem.

The cause of the problem related to improper estimation of the inversion data error by calculating the rms_{W} for each map may be due in part to measurement error. For example, where the signal-to-noise ratio is low and it is difficult to pick consistent traveltimes from individual dispersion curves, the measurement errors will be large. However, consistent biases due to modelling errors will also affect the results: these will not be represented within our uncertainty estimates yet will contribute to the misfit in eq. (1). We cannot resolve the discussion of which is the dominant source of error here, other than to say that the tomographic results should perhaps be interpreted with a little extra caution as the misfit is not reduced to lie within an ideal range.

The final choices of representative maps of Rayleigh wave group velocity at each period are shown in Fig. 11. At each period, there was little difference between each acceptable map located between the blue and red contour lines as in Fig. 10. In each case, we chose the map which has the smallest amount of damping and largest amount of smoothing while maintaining an acceptable rms_{W} value (staying within the red contour as in Fig. 10).

6 DISCUSSION

The Rayleigh wave group velocity maps in Fig. 11 show strong spatial variations in velocity at all periods that provide some interesting insights into the 3-D structure of the crust under the British Isles. These maps cover a large geographical area at a relatively high resolution and, as such, constitute the first surface wave tomography study of the crust under all of the British Isles as well as the first to use surface waves constructed from ambient noise. Each map in Fig. 11 shows the Rayleigh wave group velocities as absolute velocities with a range of ± 1 km s^{-1} from the average velocity at each period. This allows not only comparison of the spatial variations in velocity at a given period, but also a comparison between the different periods.

The maps at 5, 6 and 8-s periods shown in Figs 11(a), (b) and (c) are sensitive to average velocities through the shallow upper crust, down to depths of around 8, 10 and 12 km, respectively. These maps have generally good resolution across most of mainland Britain and an inversion grid of $0.125^\circ \times 0.125^\circ$ was used to compute them, meaning that we might expect to resolve structures with a minimum length-scale of 0.25°. At these periods, we find remarkable correlation between higher group velocities in areas of relative basement uplift during the late Palaeozoic and lower group velocities in areas with Mesozoic sedimentary basins. This is highlighted by Fig. 12, which shows the group velocity map at 5 s along with (a) the geological terrane boundaries, (b) areas of relative uplift and subsidence and (c) simplified surface geology.

High velocities across the Scottish Highlands of Northern Britain are consistent with the Proterozoic crystalline rocks of the Lewisian Complex and the Moine, Grampian and Dalradian groups. Within this region there is also some evidence for small spatial variations of velocity between each group, with the Lewisian rocks slightly faster than the Moine to the south and the Grampian group south of the GGF slightly faster than the Dalradian group immediately north of the Highland Boundary fault.

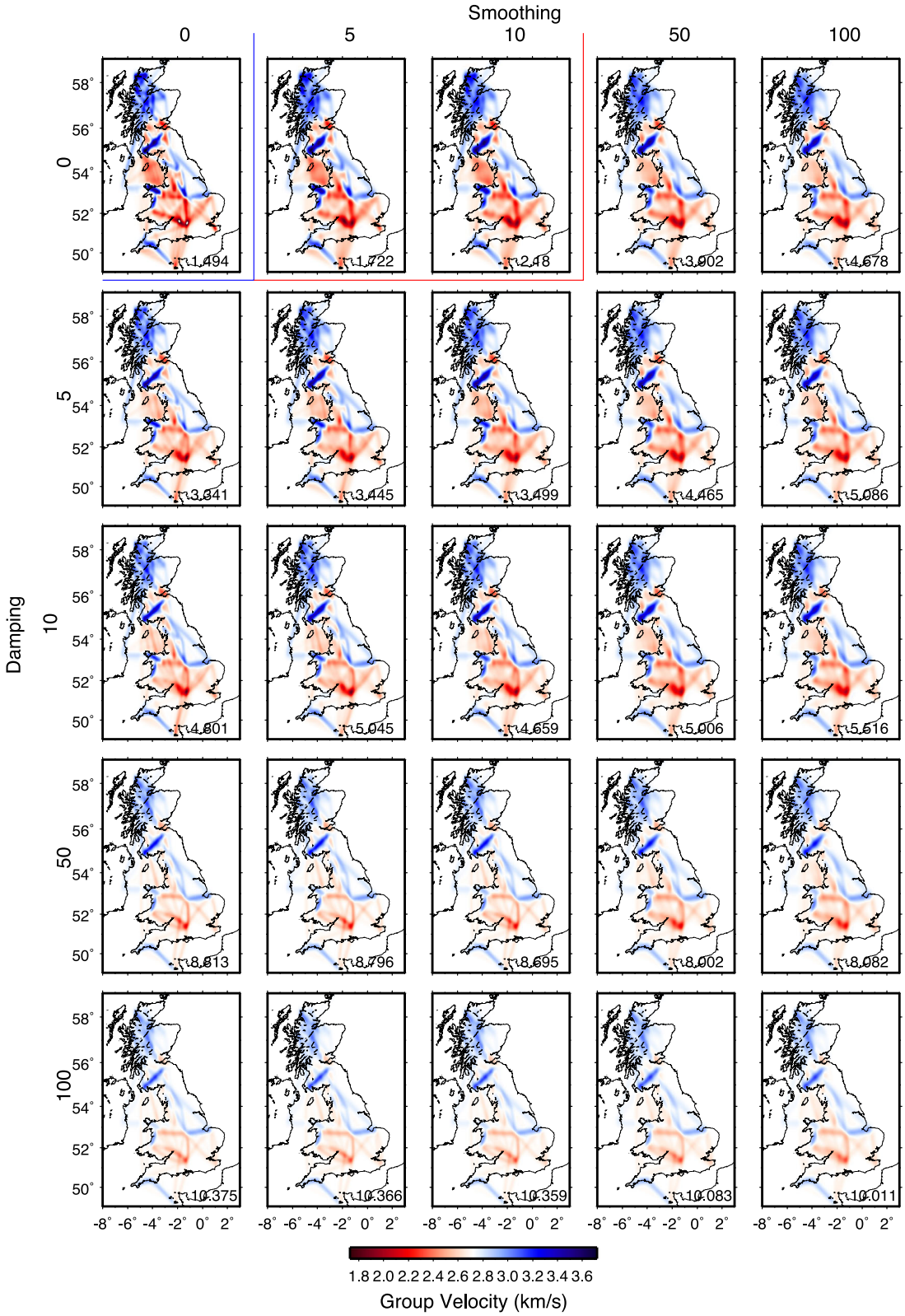

Figure 10. Rayleigh wave maps at 5-s period for different combinations of damping and smoothing values. The calculated rms_W value for each map is shown in the bottom right-hand corners. Maps located within the red contour line but outside of the blue contour are acceptable since they are geologically realistic and have an approximately acceptable rms_W value.

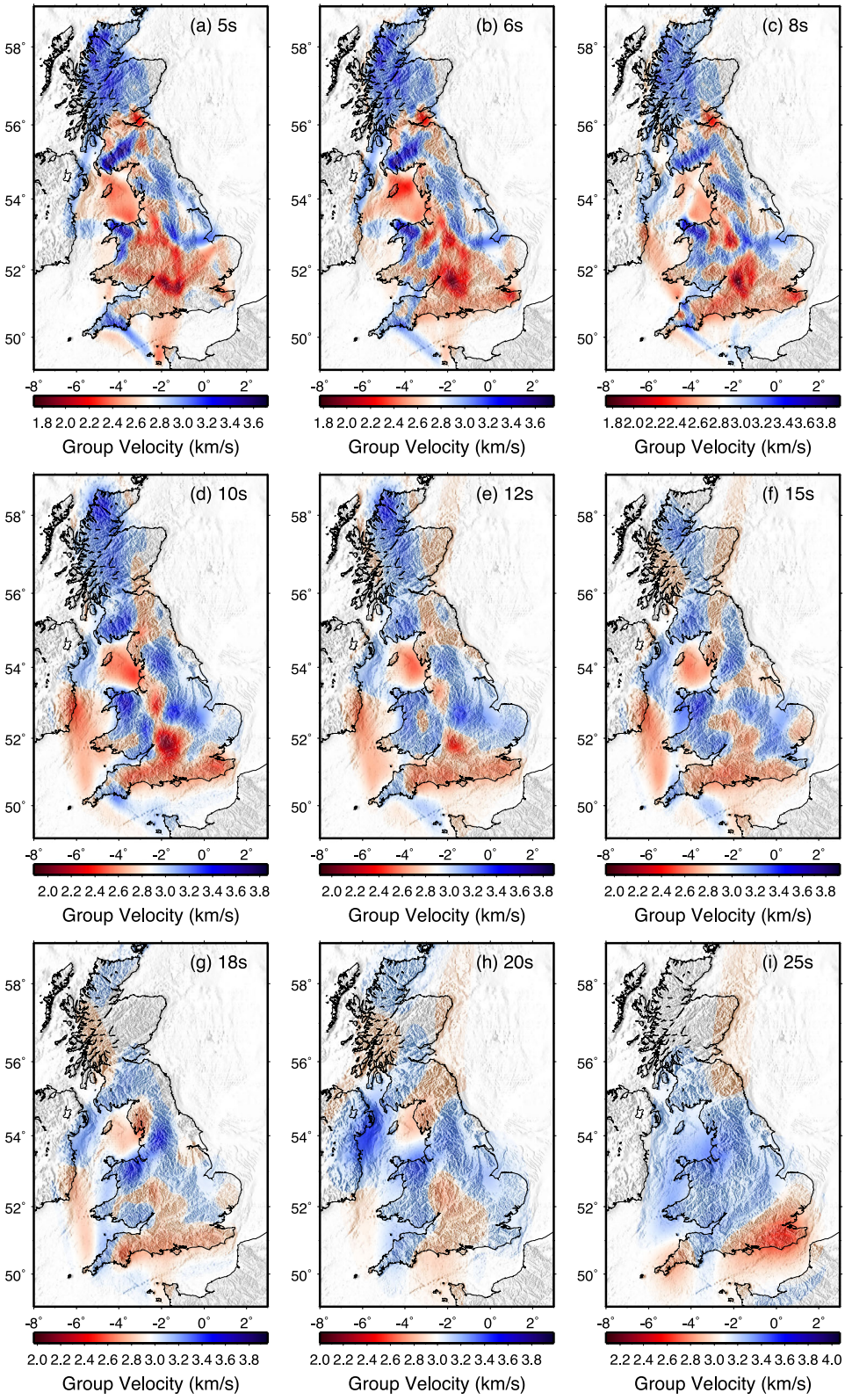

Figure 11. Rayleigh wave group velocity maps of the British Isles from cross-correlations of ambient seismic noise between the stations shown in Fig. 2 at (a) 5-s period; (b) 6-s period; (c) 8-s period; (d) 10-s period; (e) 12-s period; (f) 15-s period; (g) 18-s period; (h) 20-s period for well-constrained paths only, and at (i) 25-s period for well-constrained paths and paths with uncertainties estimated from interstation distance (since without the latter paths the tomographic results were uninterpretable due to having too few paths).

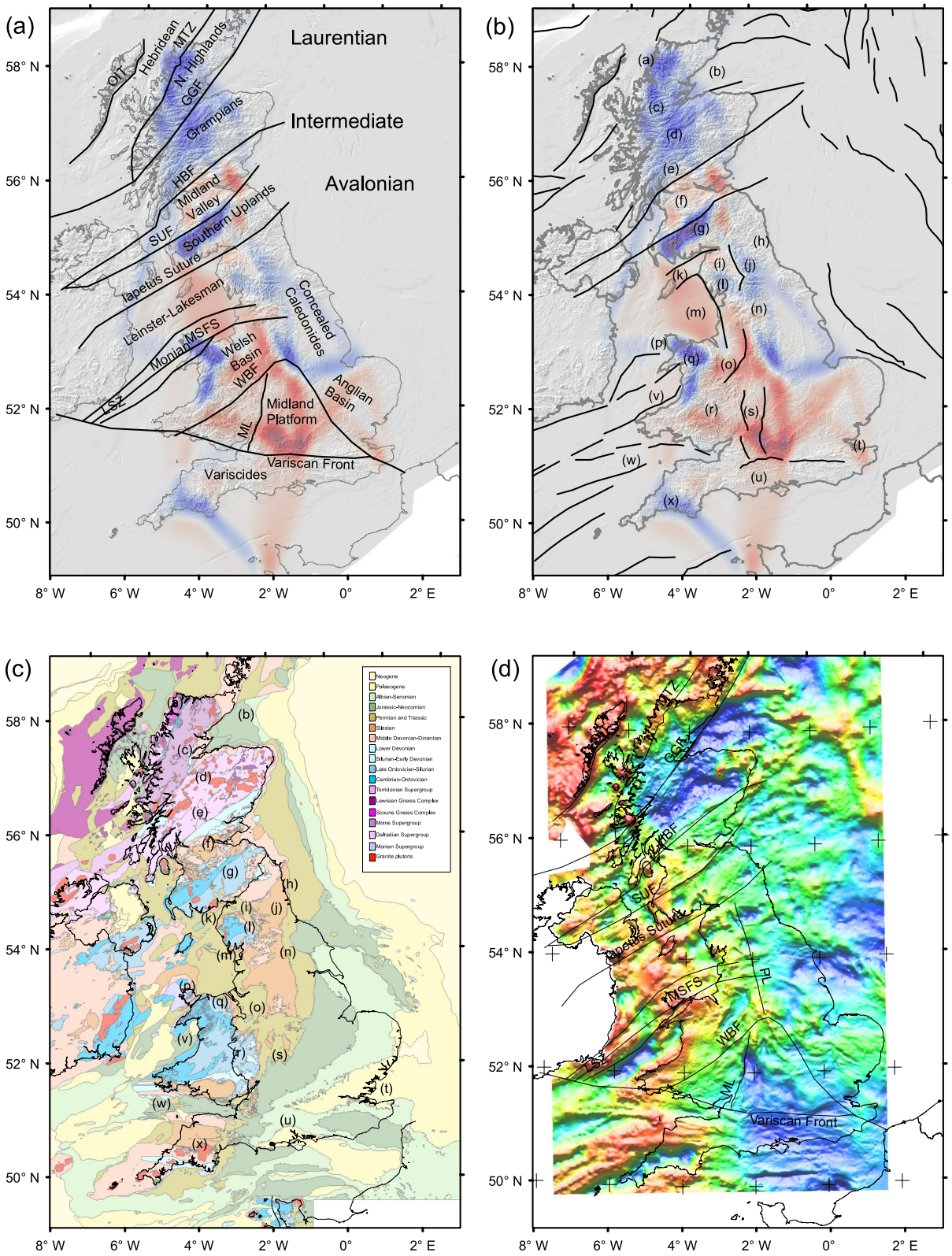

Figure 12. The group velocity map at 5 s alongside: (a) geological terrane boundaries; (b) areas of relative uplift and subsidence; (c) simplified surface geology and (d) regional gravity anomaly map. Solid black lines in (a) represent the major tectonic boundaries and fault structures as in Fig. 1. Solid black lines in (b) represent major basin bounding faults. Annotation on (b) and (c) is as follows: (a) Lewisian Complex; (b) Moray Firth Basin; (c) Moine Group; (d) Grampian Group; (e) Dalradian Group; (f) Midland Valley; (g) Southern Uplands; (h) Northumbria Basin; (i) Vale of Eden; (j) Alston Block; (k) Solway Firth Basin; (l) Lake District; (m) Irish Sea Basin; (n) Pennines; (o) Cheshire Basin; (p) Monian Group; (q) Snowdonia; (r) Welsh Massif; (s) Worcester Graben; (t) London Basin; (u) Wessex-Weald Basin; (v) Cardigan Bay; (w) Bristol Channel Basin; (x) Cornubian Massif.

South of the Highland Boundary Fault and north of the Southern Uplands Fault (SUF), an NW–SE trending low-velocity zone is consistent with the Devonian and Carboniferous rocks that form the Midland Valley sedimentary basin. In addition, the lowest velocity part of the Midland Valley occurs at its eastern end, across the Firth of Forth syncline, a known deep basin. Immediately south of the Midland Valley, a high-velocity, NW–SE trending anomaly across the Southern Uplands can be attributed to the siltstones, wackes and felsic plutons of the Southern Uplands accretionary complex. Velocities are highest in the southwest part of the Southern Uplands.

The relationship between the changes in velocity across Northern Britain and the geological terranes shown is clearly illustrated in Fig. 12(a). An area of rather lower velocity in eastern Scotland also appears to correspond to the Moray Firth Basin, although this is at the limits of the map and not well defined.

South of the Iapetus Suture line, there are areas of lower velocity that correspond to both the Solway Basin and the Vale of Eden, while the Ordovician age volcanic complex in the Lake District and the Alston Block in northeast England both correspond to areas of higher than average velocity (Figs 12b and c). The Irish Sea Basin corresponds to an extensive low-velocity region.

The late Proterozoic/Cambrian rocks of Anglesey and the Ordovician volcanic complex of Snowdonia in northwest Wales both give rise to prominent high-velocity zones (Figs 12b and c). These high velocities extend south into the Harlech dome, but are truncated to the east by low velocities that appear to be related to the thick sequence of late Ordovician/Silurian rocks that make up the Welsh Basin. Further east, areas of even lower velocity correspond to the Permo-Triassic Chesire and Worcester Basins. A particularly strong low-velocity anomaly is associated with the southern end of the Worcester Graben.

The high topography of the Pennines, running north–south through the centre of northern England is associated with a clear high-velocity feature. Immediately to the east of the Pennines there is a rather weak low-velocity region that may correspond to the Vale of York. However, resolution in this area is poorer than elsewhere and this may be an artefact.

The Midland Platform (Fig. 12a), a region of relatively undeformed Precambrian basement corresponds to an area of relatively low velocity. Chadwick & Pharaoh (1998) and Tomlinson *et al.* (2006) find that the thickness of the crust is high here. Hardwick (2008) also finds that the Midlands Platform is a region of high crustal thickness and that average crustal velocities here are lower than in the surrounding region. Similarly, our results show a persistent low-velocity anomaly in the region of the Midland Platform at most periods. Gravity data in this region (Fig. 12d) show a clear negative Bouger anomaly that could also be associated with thick crust. The area of low velocity continues to the east into the Anglian Basin and the London Basin further south.

The fast velocity region to the northeast of the Midland Platform appears to correlate with the northern limit of the Anglo-Brabant Massif (Pharaoh *et al.* 1993) in eastern England, and is colocated with a series of positive magnetic anomalies and a gravity high structure (see Fig. 12d). More detailed study is required to determine whether it is a real structural feature or an artefact of the inversion.

South of the Variscan Front, the Wessex-Weald Basin corresponds to an area of relatively low velocity. Locally high velocities are seen in the far southwest of England, coinciding with the Cornubian Massif and Hercynian granite batholiths that extend down to mid-crustal depths.

All apparent structures outside of these regions are artefacts due to smearing along interstation paths, as indicated by the resolution tests.

Figs 11(d), (e) and (f) show Rayleigh wave group velocities at 10, 12 and 15 s. These intermediate periods are most sensitive to average velocities down to depths of approximately 15–30 km. The resolution for these maps is degraded compared with the maps at 5, 6 and 8 s; therefore we expect to be able to resolve features with a minimum length-scale of around 0.5°. Strong spatial variations in group speeds are still observed at these periods, although the variability is somewhat reduced with increasing period.

The Scottish Highlands, the Southern Uplands, the Pennines, northwest Wales and Cornwall all remain associated with areas of higher than average velocities suggesting that either high velocities extend into the mid-lower crust or the maps remain dominated by high velocities at shallower depths. The fast velocities in the Southern Uplands begin to extend into Northern Ireland and the eastern Irish Sea. However, low velocities in the Midland Valley of Scotland are less pronounced at these periods, providing evidence that the sedimentary basin is underlain by a region of relatively high velocity. This is in good agreement with Dentith & Hall (1989, 1990), who find evidence from seismic refraction studies across the Midland Valley, that approximately 4–8 km of sediment overlies high-velocity basement rocks. A high-velocity anomaly east of the Midlands Platform can also still be observed on the intermediate period maps.

Low-velocity anomalies that coincide with the Mesozoic Basins in the Irish Sea, Chester, Worcester and Wessex remain present at 10, 12 and 15 s, however, the amplitude of these low velocity anomalies appears to decrease with increasing period, which might suggest that group velocities at these periods remain dominated by the low velocities at shallower depths. An area of low velocity is also apparent in the southern Irish Sea.

The 20 and 25-s maps shown in Figs 11(h) and (i) are sensitive to average velocities to depths of approximately 32 and 38 km, respectively. Both these maps may be sensitive to the changing depth of the Moho (since for a shallow Moho, more high-velocity mantle material will be included within this depth range).

Fast velocities continue to dominate in Northern Ireland and the eastern Irish Sea, spreading west into the Southern Upland, the Isle of Man and North Wales, although a persistent weak low-velocity zone continues to coincide with the Irish Sea Basin further to the east. These high velocities may provide some further evidence for the underplating in the lower crust suggested by Al-Kindi *et al.* (2003) and also observed by Kelly *et al.* (2007), Hardwick (2008) and Davis *et al.* (2012). The high-velocity anomaly at 25 s also correlates well with a gravity high down the west side of the British Isles (Fig. 12d).

A low-velocity anomaly appears in the west of Scotland at periods of 15, 18 and 20 s, that coincides with an area of major volcanic activity during the Atlantic rifting episode in the Tertiary, and includes the volcanic complexes of Skye, Mull and Rum. However, there is little supporting evidence for the presence of such a low-velocity anomaly.

Low velocities are still seen across the Midland Platform though this disappears with increasing period. The pronounced low velocities seen in the 25-s map in southeast England can be related to the relatively high thickness of the crust found in this area by a number of studies, for example, Chadwick & Pharaoh (1998). The depth of the Moho decreases to the northwest which is in agreement with the slight increase in observed velocities in a northwest direction,

and with the two depth inversions shown in Fig. 8. The lower than average velocities observed to the east of the Midland Valley and eastern Scotland may also be related to thick crust in this region, however, the spatial extend of this anomaly is rather larger than expected.

Lin *et al.* (2006) show that it is possible to obtain interferometric surface waves across an ocean basin. They present year-long cross-correlations of ambient seismic noise between continental and oceanic island stations across the Pacific Ocean. The resulting surface waves prove that seismic noise is also coherent over long oceanic paths, as it is over continental paths. These results led us to postulate that passive seismic interferometry and ambient noise tomography may be possible across the North Sea. However, we were generally unable to construct good quality, interferometric surface waves for paths crossing the North Sea.

The problems observed in this study regarding cross-North Sea paths may be due to the well-documented *Lg* wave blockage in the central and northern North Sea observed by Gregersen (1984) and Kennett *et al.* (1985) and modelled by Maupin (1989). Alternatively, the poor construction of interferometric surface waves for these paths may be due to the cross-correlation method that we have applied. We have assumed that the dominant source of noise in this study is the Atlantic Ocean; however, the North Sea may also be a significant source of microseismic noise. This may be a reason why interferometric surface waves are poorly reconstructed for cross-North Sea paths. Say that the signal due to a seismic source located between two receivers is recorded at those receivers. If the two recordings are cross-correlated, their phases (and hence traveltimes) are subtracted. This results in energy in the cross-correlogram that arrives at either positive or negative times before the arrival of any physical surface wave. This may explain the occurrence of noise in the seismograms in Fig. 6 before the time when a surface wave should arrive.

Finally, our study focused on group velocity measurements rather than phase velocity, which is known to be more accurate (Lin *et al.* 2008). We plan to address this in future work as well as carry out depth inversions across the study area.

7 CONCLUSIONS

In this paper, we have shown that seismic interferometry can be applied successfully to construct surface waves across the British Isles using only ambient seismic noise. We have presented the first Rayleigh wave group velocity maps across the British Isles using the ambient noise tomography method. These maps show excellent agreement with many of the geological features of the British Isles. At short periods, the maps show low velocities in Palaeozoic sedimentary basins such as the Midland Valley and the Welsh basin, as well as areas of Mesozoic subsidence such as the Irish Sea Basin, the Cheshire Basin, the Worcester Graben and the Wessex Basin at both short and intermediate periods. High-velocity anomalies occur predominantly in areas of exposed Proterozoic basement such as the Scottish Highlands and northwest Wales, areas of late Palaeozoic uplift such as the Southern Uplands and the Pennines, and the Ordovician volcanic centres of Snowdonia and the Lake District.

Interestingly, our maps show a persistent, robust low-velocity anomaly in the region of the Midlands Platform, a wedge-shaped basement block of Proterozoic crust that dominates much of Southern Britain. This result is consistent with other observations and with the interpretation that crustal thickness is high and that average velocities here are lower than the surrounding region.

At longer periods, which are sensitive to velocities in the lower crustal/upper mantle, the maps suggest that the depth of Moho beneath the British Isles decreases towards the north and west. Areas of fast velocity in the lower crust also coincide with areas thought to be associated with underplating of the lower crust such as Northern Ireland, the eastern Irish Sea and northwest Wales. The extent of the region of higher velocity correlates well with the locations of British earthquakes, and is consistent with previous studies which suggest that British seismicity might be influenced by either mantle upwelling beneath the west of the British Isles (Bott & Bott 2004; Arrowsmith *et al.* 2005), or by internal loading due to irregular mass distribution (underplate) (Maguire *et al.* 2011).

ACKNOWLEDGEMENTS

Thanks to the IRIS Data Management Centre, the AWE Blacknest UKNet array, the British Isles Seismic Experiment and ORFEUS who provided some of the seismic data used in this study. Many of the figures in this paper were prepared using GMT (Wessel & Smith 1995). We also thank the British Geological survey which partly funded HN's PhD.

REFERENCES

Aki, K. & Richards, P., 2002. *Quantitative Seismology,* 2nd edn, University Science Books.

Al-Kindi, S., White, N., Sinha, M., England, R. & Tiley, R., 2003. Crustal trace of a hot convective sheet, *Geology,* **31,** 207–210.

Anell, I., Thybo, H. & Artemieva, I., 2009. Cenozoic uplift and subsidence in the North Atlantic region: geological evidence revisited, *Tectonophysics*, **474**(1–2), 78–105.

Arroucau, P., Rawlinson, N. & Sambridge, M., 2010. New insight into Cainozoic sedimentary basins and Palaeozoic suture zones in southeast Australia from ambient noise surface wave tomography, *Geophys. Res. Lett.,* **37,** L07303, doi:10.1029/2009GL041974.

Arrowsmith, S., Kendall, M., White, N., VanDecar, J. & Booth, D., 2005. Seismic imaging of a hot upwelling beneath the British Isles, *Geology,* **33**(5), 345–348.

Asencio, E., Knapp, J., Owens, T. & Helffrich, G., 2003. Mapping fine-scale heterogeneities within the continental mantle lithosphere beneath Scotland: combining active and passive source seismology, *Geology,* **31,** 447–480.

Bamford, D., Nunn, K., Prodehl, C. & Jacob, B., 1978. LISPB IV. Crustal structure of northern Britain, *Geophys. J. R. astr. Soc.,* **54,** 43–60.

Barton, P., 1992. LISPB revisited: a new look under the Caledonides of northern Britain, *Geophys. J. Int.,* **110,** 371–391.

Bastow, I., Owens, T., Helffrich, G. & Knapp, J., 2007. Spatial and temporal constraints on sources of seismic anisotropy: evidence from the Scottish highlands, *Geophys. Res. Lett.,* **34**(5), doi:10.1029/2006GL028911.

Behr, Y., Townend, J., Bannister, S. & Savage, M.K., 2010. Shear velocity structure of the Northland Peninsula, New Zealand, inferred from ambient noise correlations, *J. geophys. Res.,* **115,** B05309, doi:10.1029/2009JB006737.

Bensen, G., Ritzwoller, M., Barmin, M., Levshin, A., Moschetti, M., Shapiro, N. & Yang, Y., 2007. Processing seismic ambient noise data to obtain reliable broad-band surface wave dispersion measurements, *Geophys. J. Int.,* **169,** 1239–1260.

Bensen, G.D., Ritzwoller, M.H. & Shapiro, N.M., 2008. Broadband ambient noise surface wave tomography across the United States, *J. geophys. Res.,* **113**(B5), 1–21.

Bijwaard, H. & Spakman, W., 1999. Tomographic evidence for a narrow whole mantle plume below Iceland, *Earth planet. Sci. Lett.,* **166,** 121–126.

Bluck, B.J., Gibbons, W. & Ingham, J.K., 1992. Terranes, in *Atlas of Palaeogeography and Lithofacies,* pp. 1–4, eds Cope, J.C., Ingham, J.K. & Rawson, P.F., Geological Society of London Memoirs, No. 13.

Bott, M. & Bott, J., 2004. The Cenozoic uplift and earthquake belt of mainland Britain as a response to an underlying hot, low-density upper mantle, *J. geol. Soc. Lond.,* **161,** 19–29.

Bott, M.H.P., Long, R.E., Green, A.S.P., Lewis, A.H.J., Sinha, M.C. & Stevenson, D.L., 1985. Crustal structure south of the Iapetus suture beneath northern England, *Nature,* **314,** 724–727.

Brodie, J. & White, N., 1994. Sedimentary basin inversion caused by igneous underplating: northwest European continental shelf, *Geology,* **22**(2), 147–150.

Campillo, M. & Paul, A., 2003. Long-range correlations in the diffuse seismic coda, *Science,* **299**(5606), 547–549.

Chadwick, R. & Pharaoh, T., 1998. The seismic reflection Moho beneath the United Kingdom and adjacent areas, *Tectonophysics,* **299,** 255–279.

Cho, K., Herrmann, R., Ammon, C. & Lee, K., 2007. Imaging the upper crust of the Korean Peninsula by surface-wave tomography, *Bull. seism. Soc. Am.,* **97**(1B), 198–207.

Curtis, A. & Halliday, D., 2010. Source-receiver wave field interferometry, *Phys. Rev. E,* **81,** 046601, doi:10.1103/PhysRevE.81.046601.

Curtis, A., Gerstoft, P., Sato, H., Snieder, R. & Wapenaar, K., 2006. Seismic interferometry—turning noise into signal, *Leading Edge,* **25**(9), 1082–1092.

Curtis, A., Trampert, J., Snieder, R. & Dost, B., 1998. Eurasian fundamental mode surface wave phase velocities and their relationship with tectonic structures, *J. geophys. Res.,* **103**(B11), 26 919–26 947.

Curtis, A., Nicolson, H., Halliday, D., Trampert, J. & Baptie, B., 2009. Virtual seismometers in the subsurface of the Earth from seismic interferometry, *Nature Geosci.,* **2**(10), 700–704.

Curtis, A., Behr, Y., Entwistle, E., Galetti, E., Townend, J. & Bannister, S., 2012. The benefit of hindsight in observational science: retrospective seismological observations, *Earth planet. Sci. Lett.,* **345–348,** 212–220.

Davis, M., 2010. A receiver function study of the crust and mantle beneath the British Isles, *PhD thesis,* University of Cambridge.

Davis, M., White, N., Priestly, K., Baptie, B. & Tilmann, F., 2012. Crustal structure of the British Isles and its epeirogenic consequences, *Geophys. J. Int.,* **190**(2), 705–725.

Dentith, M. & Hall, J., 1989. MAVIS: an upper crustal seismic refraction experiment in the Midland Valley of Scotland, *Geophys. J. Int.,* **99,** 627–643.

Dentith, M. & Hall, J., 1990. MAVIS: geophysical constraints on the structure of the Carboniferous basin of West Lothian, *Trans. R. Soc. Edinburgh,* **81,** 117–126.

Di Leo, J., Bastow, I. & Helffrich, G., 2009. Nature of the Moho beneath the Scottish Highlands from a receiver function perspective, *Tectonophysics,* **474,** 214–222

Douglas, A., 2001. The UK broadband seismology network, *Astr. Geophys.,* **42,** 2.19–2.21.

Edwards, J.W.F. & Blundell, D.J., 1984. *Summary of seismic refraction experiments in the English Channel, Celtic Sea and St. George's Channel,* British Geological Survey Marine Geophysics Report No. 144.

Foulger, G., 2002. Plumes, or plate tectonic processes? *Astron. Geophys.,* **43,** 6.19–6.23.

Fry, B., Boschi, L., Ekstrom, G. & Giardini, D., 2008. Europe-Mediterranean tomography: high correlation between new seismic data and independent geophysical observables, *Geophys. Res. Lett.,* **35,** L04301, doi:10.1029/2007GL031519.

Galetti, E. & Curtis, A., 2012. Generalised receiver functions and seismic interferometry, *Tectonophysics,* **532–535,** 1–26.

Gregersen, S., 1984. Crustal structure anomalies detected with Lg waves in grabens near continenal margins in Greenland and in the North Sea, *Mar. Geophys. Res.,* **6,** 409–413.

Gudmundsson, Ó., Khan, A. & Voss, P., 2007. Rayleigh-wave group-velocity of the Icelandic crust from correlation of ambient seismic noise, *Geophys. Res. Lett.,* **34,** L14314, doi:10.1029/2007GL030215.

Halliday, D. & Curtis, A., 2010. An interferometric theory of source-receiver scattering and imaging, *Geophysics,* **75**(6), SA95–SA103.

Hardwick, A., 2008. New insights into the crustal structure of the England, Wales and Irish Seas areas from local earthquake tomography and associated seismological studies, *PhD thesis,* University of Leicester.

Herrmann, R., 2005, *Computer Programs in Seismology,* Version 3.30, St Louis University.

Hillis, R.R. *et al.*, 2008. Cenozoic exhumation of the southern British Isles, *Geology,* **36,** 371–174.

Hong, T. & Menke, W., 2006. Tomographic investigation of the wear along the San Jacinto fault, southern California, *Phys. Earth planet. Inter.,* **155**(3–4), 236–248.

Jacob, A.B.W., Kaminski, W., Murphy, T., Phillips, W.E.A. & Prodehl, C., 1985, A crustal model for a northeast-southwest profile through Ireland, *Tectonophysics,* **113**(1–2), 75–103.

Kang, T.-S. & Shin, J., 2006. Surface-wave tomography from ambient seismic noise of accelerograph networks in southern Korea, *Geophys. Res. Lett.,* **33,** L17303, doi:10.1029/2006GL027044.

Kelly, A., England, R. & Maguire, P., 2007. A Crustal seismic velocity model for the UK, Ireland and surrounding seas, *Geophys. J. Int.,* **171**(3), 1172–1184.

Kennett, B., Gregersen, S., Mykkeltveit, S. & Newmark, R., 1985. Mapping of crustal heterogeneity in the North Sea basin via the propagation of Lg-waves, *Geophys. J. R. astr. Soc.,* **83,** 299–306.

Kennett, B., Sambridge, M. & Williamson, P., 1988. Subspace methods for large inverse problems with multiple parameter classes, *Geophys. J. Int.,* **94,** 237–247.

Kirstein, L. & Timmerman, M., 2000. Evidence of the proto-Iceland plume in northwestern Ireland at 42 Ma from helium isotopes, *J. Geol. Soc.,* **157**(5), 923–928.

Lawrence, J. & Prieto, G., 2011. Attenuation tomography of the western United States from ambient seismic noise, *J. geophys. Res.,* **116,** B06302, doi:10.1029/2010JB007836.

Li, H., Su, W., Wang, C.W. & Huang, Z., 2009. Ambient noise Rayleigh wave tomography in western Sichuan and eastern Tibet, *Earth planet. Sci. Lett.,* **282,** 201–211.

Liang, C. & Langston, C., 2008. Ambient seismic noise tomography and structure of eastern North America, *J. geophys. Res.,* **113,** B03309, doi:10.1029/2007JB005350.

Lin, F., Ritzwoller, M. & Shapiro, N., 2006. Is ambient noise tomography across ocean basins possible? *Geophys. Res. Lett.,* **33,** L14304, doi:10.1029/2006GL026610.

Lin, F., Moschetti, M. & Ritzwoller, M., 2008. Surface wave tomography of the western United States from ambient seismic noise: Rayleigh and Love wave phase velocity maps, *Geophys. J. Int.,* **173,** 281–298.

Lin, F., Ritzwoller, M., Townend, J., Bannister, S. & Savage, M., 2007. Ambient noise Rayleigh wave tomography of New Zealand, *Geophys. J. Int.,* **170,** 649–666.

Luzon, F., Almendros, J. & Garcia-Jerez, A., 2011. Shallow structure of Deception Island, Antarctica, from correlations of ambient seismic noise on a set of dense seismic arrays, *Geophys. J. Int.,* **185,** 737–748.

Maguire, P., England, R. & Hardwick, A., 2011. LISPB DELTA, a lithospheric seismic profile in Britain: analysis and interpretation of the Wales and southern England section, *J. geol. Soc.,* **168,** 61–82.

van-Manen, D., Curtis, A. & Robertsson, J., 2006. Interferometric modeling of wave propagation in inhomogeneous elastic media using time reversal and reciprocity, *Geophysics,* **71**(4), SI47–SI60.

van-Manen, D., Robertsson, J. & Curtis, A., 2005. Modeling of wave propagation in inhomogeneous media, *Phys. Rev. Lett.,* **94,** 164 301–164 304.

van-Manen, D., Robertsson, J. & Curtis, A., 2007. Exact wavefield simulation for finite-volume scattering problems, *J. acous. Soc. Am.,* **122**(4), 115–121.

Marquering, H. & Snieder, R., 1996. Surface-wave velocity structure beneath Europe, the northeastern Atlantic and western Asia from waveform inversion including surface wave mode coupling, *Geophys. J. Int.,* **127,** 238–304.

Maupin, V., 1989. Numerical modelling of Lg wave propagation across the North Sea Central Graben, *Geophys. J. Int.,* **99,** 273–283.

Moschetti, M., Ritzwoller, M. & Shapiro, N., 2007. Surface wave tomography of the western United States from ambient seismic noise: Rayleigh wave group velocity maps, *Geochem. Geophys. Geosyst.,* **8,** Q08010, doi:10.1029/2007GC001655.

Nadin, P., Kusznir, N. & Cheadle, M., 1997. Early Tertiary plume uplift of the North Sea and Faeroe-Shetland Basins, *Earth planet. Sci. Lett.,* **148,** 109–127.

Nadin, P., Kusznir, N. & Toth, J., 1995. Transient regional uplift in the Early Tertiary of the northern North Sea and the development of the Iceland Plume, *J. geol. Soc.,* **152,** 953–958.

Nicolson, H., Curtis, A., Baptie, B. & Galetti, E., 2012. Seismic interferometry and ambient noise tomography in the British Isles, *Proc. geol. Assoc.,* **123,** 74–86.

Pawlack, A., Eaton, D., Bastow, I., Kendall, J., Hellfrich, G., Wookey, J. & Snyder, D., 2010. Crustal structure beneath Hudson Bay from ambient-noise tomography: implications for basin formation, *Geophys. J. Int.,* **184,** 65–82.

Peter, D., Boschi, L., Deschamps, F., Fry, B., Ekström, G. & Giardini, D., 2008. A new finite-frequency shear-velocity model of the European-Mediterranean region, *Geophys. Res. Lett.,* **35,** L16315, doi:10.1029/2008GL034769.

Pharaoh, T.C., Molyneux, S.G., Merriman, R.J., Lee, M.K. & Verniers, J., 1993. The Caledonides of the Anglo-Brabant Massif reviewed, *Geological Magazine,* **130,** 561–562.

Pilidou, S., Priestley, K., Gudmundsson, Ó. & Debayle, E., 2004. Upper mantle S-wave speed heterogeneity and anisotropy beneath the North Atlantic from regional surface wave tomography: the Iceland and Azores plume, *Geophys. J. Int.,* **159,** 1057–1076.

Poliannikov, O. & Willis, M., 2011. Interferometric correlogram-space analysis, *Geophysics,* **76,** 1, SA9-SA17.

Pyle, M., Wiens, D., Nyblade, A. & Anandakrishnan, S., 2010. Crustal structure of the Transantarctic Mountains near the Ross Sea from ambient seismic noise tomography, *J. geophys. Res.,* **115,** B11310, doi:10.1029/2009JB007081.

Rawlinson, N., Reading, A. & Kennett, B., 2006. Lithospheric structure of Tasmania from a novel form of teleseismic tomography, *J. geophys. Res.,* **111**(B2), B02301, doi:10.1029/2005JB003803.

Rawlinson, N., Sambridge, M. & Saygin, E., 2008. A dynamic objective function technique for generating multiple solution models in seismic tomography, *Geophys. J. Int.,* **174,** 295–308.

Ritzwoller, M. & Levshin, A., 1998. Eurasian surface wave tomography: group velocities, *J. geophys. Res.,* **103**(B3), 4839–4878.

Ritzwoller, M., Lin, F. & Shen, W., 2011. Ambient noise tomography with a large seismic array, *C. R. Geosci.,* **343**(8–9), 558–570.

Ritzwoller, M.H., Shapiro, N.M., Barmin, M.P. & Levshin, A.L., 2002. Global surface wave diffraction tomography, *J. geophys. Res.,* **107**(B12), 2156–2202.

Russell, D., 1987. Multi-channel processing of dispersed surface waves, *PhD thesis,* University of St Louis.

Sabra, K., Gerstoft, P., Roux, P., Kuperman, W. & Fehler, M., 2005. Surface wave tomography from microseisms in Southern California, *Geophys. Res. Lett.,* **32,** L14311, doi:10.1029/2005gl023155.

Saygin, E. & Kennett, B., 2010. Ambient seismic tomography of Australian continent, *Tectonophysics,* **481,** 116–125.

Schivardi, R. & Morelli, A., 2009. Surface wave tomography in the European and Mediterranean region, *Geophys. J. Int.,* **177,** 1050–1066.

Sethian, J. & Popovici, A., 1999. 3-D traveltime computation using the fast marching method, *Geophysics,* **64**(2), 516–523.

Shapiro, N., Campillo, M., Stehly, L. & Ritzwoller, M., 2005. High-resolution surface-wave tomography from ambient seismic noise, *Science,* **307**(5715), 1615–1618.

Slob, E., Draganov, D. & Wapenaar, K., 2007. Interferometric electromagnetic Green's functions representations using propagation invariants, *Geophys. J. Int.,* **169,** 60–80.

Snieder, R., 2004. Extracting the Green's function from the correlation of coda waves: a derivation based on stationary phase, *Phys. Rev. E,* **69,** 046610, doi:10.1103/PhysRevE.69.046610.

Snieder, R., 2007. Extracting the Green's function of attenuating heterogeneous media from uncorrelated waves, *J. acous. Soc. Am.,* **121,** 2637–2643.

Tomlinson, J.P., Denton, P., Maguire, P.K.H. & Booth, D.C., 2006. Analysis of the crustal velocity structure of the British Isles using teleseismic receiver functions, *Geophys. J. Int.,* **167,** 223–237.

Tonegawa, T. & Nishida, K., 2010. Inter-source body wave propagations derived from seismic interferometry, *Geophys. J. Int.,* **183,** 861–868.

Trampert, J. & Snieder, R., 1996. Model estimations biased by truncated expansions: possible artifacts in seismic tomography, *Science,* **271,** 1257–1260.

Villaseñor, A., Ritzwoller, M., Levshin, A., Barmin, M., Engdahl, E., Spakman, W. & Trampert, J., 2001. Shear velocity structure of central Eurasia from inversion of surface wave velocities, *Phys. Earth planet. Inter.,* **123,** 169–184.

Villaseñor, A., Yang, Y., Ritzwoller, Michael H. & Gallart, J., 2007. Ambient noise surface wave tomography of the Iberian Peninsula: implications for shallow seismic structure, *Geophys. Res. Lett.,* **34**(11), 1–5.

Wapenaar, K., 2003. Synthesis of an inhomogeneous medium from its acoustic transmission response, *Geophysics,* **68**(5), 1756–1759.

Wapenaar, K., 2004. Retrieving the elastodynamic Green's function of an arbitrary homogeneous medium by cross correlation, *Phys. Rev. E,* **93,** 254301, doi:10.1103/PhysRevLett.93.254301.

Wapenaar, K. & Fokkema, J., 2006. Green's function representations for seismic interferometry, *Geophysics,* **71,** S133–S144.

Wapenaar, K., Draganov, D., Snieder, R., Campman, X. & Verdel, A., 2010a. Tutorial on seismic interferometry. Part I: basic principles, *Geophysics,* **75**(5), 195–209.

Wapenaar, K., Slob, E., Snieder, R. & Curtis, A., 2010b. Tutorial on seismic interferometry. Part II: underlying theory and new advances, *Geophysics,* **75**(5), 211–227.

Wapenaar, K., Ruigrok, E., van der Neut, J. & Draganov, D., 2011. Improved surface-wave retrieval from ambient seismic noise by multi-dimensional deconvolution, *Geophys. Res. Lett.,* **38,** L01313, doi:10.1029/2010GL045523.

Weidle, C. & Maupin, V., 2008. An upper-mantle S-wave velocity model for Northern Europe from Love and Rayleigh group velocities, *Geophys. J. Int.,* **175,** 1154–1168.

Wessel, P. & Smith, W., 1995. New version of the generic mapping tools released, *EOS,Trans. Am. geophys. Un.,* **72,** 329.

Woodcock, N. & Strachan, R., 2000, *Geological History of Britain and Ireland,* Blackwell Science.

Yang, Y., Ritzwoller, M., Levshin, A. & Shapiro, N., 2007. Ambient noise Rayleigh wave tomography across Europe, *Geophys. J. Int.,* **168,** 259–274.

Yang, Y., Li, A. & Ritzwoller, M., 2008. Crustal and uppermost mantle structure in southern Africa revealed from ambient noise and teleseismic tomography, *Geophys. J. Int.,* **174,** 235–248.

Yao, H. & van der Hilst, R., 2009. Analysis of ambient noise energy distribution and phase velocity bias in ambient noise tomography, with application to SE Tibet, *Geophys. J. Int.,* **179,** 1113–1132.

Yao, H., van der Hilst, R. & de Hoop, M., 2006. Surface-wave array tomography in SE Tibet from ambient seismic noise and two-station analysis—I. Phase velocity maps, *Geophys. J. Int.,* **166,** 732–744.

Yao, H., Beghein, C. & van der Hilst, R., 2008. Surface wave array tomography in SE Tibet from ambient seismic noise and two-station analysis—II. Crustal and upper-mantle structure, *Geophys. J. Int.,* **173,** 205–219.

Yao, H., Gouédard, P., Collins, J., McGuire, J. & van der Hilst, R., 2011. Structure of young East Pacific Rise lithosphere from ambient noise correlation analysis of fundamental- and higher-mode Scholte waves, *C. R. Geosci.,* **343,** 571–583.

Zheng, S., Sun, X., Song, X., Yang, Y. & Ritzwoller, M., 2008. Surface wave tomography of China from ambient seismic noise correlation, *Geochem. Geophys. Geosyst.,* **9,** Q05020, doi:10.1029/2008GC001981.

Zheng, X., Jiao, W., Zhang, C. & Wang, L., 2010. Short-period Rayleigh-wave group velocity tomography through ambient noise cross-correlation in Xinjiang, Northwest China, *Bull. seism. Soc. Am.,* **100,** 1350–1355.